

Angular Momentum Transfer in a Protolunar Disk

Takaaki Takeda

Department of Earth and Planetary Sciences, Tokyo Institute of Technology

2-12-1 Ookayama, Meguro-ku, Tokyo 152-8551, Japan

ttakeda@geo.titech.ac.jp

and

Shigeru Ida

Department of Earth and Planetary Sciences, Tokyo Institute of Technology

2-12-1 Ookayama, Meguro-ku, Tokyo 152-8551, Japan

ida@geo.titech.ac.jp

ABSTRACT

We numerically calculated angular momentum transfer processes in a dense particulate disk within Roche limit by global N -body simulations, up to $N = 10^5$, for parameters corresponding to a protolunar disk generated by a giant impact on a proto-Earth. In the simulations, both self-gravity and inelastic physical collisions are included. We first formalized expressions for angular momentum transfer rate including self-gravity and calculated the transfer rate with the results of our N -body simulations. Spiral structure is formed within Roche limit by self-gravity and energy dissipation of inelastic collisions, and angular momentum is effectively transferred outward. Angular momentum transfer is dominated by both gravitational torque due to the spiral structure and particles' collective motion associated with the structure. Since formation and evolution of the spiral structure is regulated by the disk surface density, the angular momentum transfer rate depends on surface density, but not on particle size or number, so that the time scale of evolution of a particulate disk is independent on the number of particles (N) that is used to represent the disk, if N is large enough to represent the spiral structure. With $N = 10^5$, the detailed spiral structure is resolved while it is only poorly resolved with $N = 10^3$, however, we found that calculated angular momentum transfer does not change as long as $N \gtrsim 10^3$.

Subject headings: accretion disks—Moon—planets and satellites: formation—planets: rings

1. INTRODUCTION

Angular momentum transfer is essential in evolution and structure formation of accretion disks, such as galactic, protoplanetary disks, and planetary rings. As angular momentum is transferred outward, inner material falls to the central body and outer material migrate outward (Lynden-bell & Pringle 1974). In a particulate disk within Roche limit such as a planetary ring or a protolunar disk (see below), angular momentum is transferred through mutual collisions and self-gravitational interactions. In the present paper, we focus on angular momentum transfer in such a disk, in particular, a protolunar disk.

“Giant Impact Hypothesis” for the origin of the Moon (Hartmann & Davis 1975; Cameron & Ward 1976) assumes that a Mars-sized protoplanet collided with the early Earth, some fraction of the impactor’s mantle materials were flung away to form a circumterrestrial debris disk (a protolunar disk), and the Moon accreted from the disk. Within Roche limit, which is about three Earth radii, accretion of large bodies is inhibited by the tidal effect from the Earth, and only materials beyond the Roche limit can form the Moon (e.g., Canup & Esposito (1995)). Therefore outward mass transfer from the Roche limit regulates the time scale of lunar formation (Ida, Canup, & Stewart 1997; hereafter referred to as ICS97), if most materials in the protolunar disk are initially confined within Roche limit. ICS97 followed the evolution of a protolunar disk by direct N -body simulations with $N = 1,000$ - $3,000$. More detailed calculations were performed by Kokubo, Ida & Makino (2000; hereafter KIM00) with $N = 10,000$. ICS97 and KIM00 found that lunar formation time scale is very short (\sim a month to a year) after condensation of disk materials. As the protolunar disk evolves, density spiral arms are quickly developed within Roche limit. KIM00 suggested that the spiral arms regulate the angular momentum transfer. Also, in the local N -body simulations of Saturn’s ring, Salo (1995; hereafter S95) and Daisaka & Ida (1999; hereafter DI99) show similar wake-like structure.

When such structure develops, disk particles move collectively. The motion depends on surface density of the disk, independent of individual particle sizes, as shown later. If collective motion regulates angular momentum transfer, the results in N -body simulations would be independent of how many particles are used for simulations, as long as particle number is enough to resolve the spiral structure. Both physical collisions and self-gravity play important roles in the formation of the structure (S95; DI99).

Angular momentum transfer in a planetary ring has mostly been studied in a non-self gravitating system assuming spatial uniformity. Goldreich & Tremaine (1978; hereafter GT78) analytically solved the Boltzmann equation and derived an angular momentum transfer rate on the analogy of molecular viscosity. Araki & Tremaine (1986; hereafter AT86) included the effect of finite size of particles. During a physical collision, angular momentum is

transferred from one particle to another by compressive waves through interior of particles. They showed that this type of angular momentum transfer is dominant when spatial density of particles is high enough (see section 3.1). Wisdom & Tremaine (1988; hereafter WT88) formulated the angular momentum transfer in a particle disk in local coordinates, taking into account physical collisions, and numerically simulated a particle disk to calculate the transfer rate. Their results are in good agreement with those by GT78 and AT86. Petit & Greenberg (1996) also showed similar results, numerically calculating evolution of velocity ellipsoid.

When self-gravity is included, the particles are no longer distributed uniformly (Richardson 1994; S95; DI99). Borderies, Goldreich & Tremaine (1983) included the perturbation by a satellite and investigated the dynamics near a resonance, and Borderies, Goldreich & Tremaine (1985) derived formula for angular momentum transfer by self-gravity with stream line approximation for a ring. Angular momentum transfer due to gravitational torque has been studied also in spiral galaxies or star formation. With trailing spirals, the angular momentum is transferred outward according to the amplitude and wavenumber of the spirals (Lynden-Bell & Kalnajs 1972). The torque exerted by the spirals transfers angular momentum effectively (Larson 1984). However, the theories for galaxies do not include physical collisions.

Ward & Cameron (1978) argued the evolution of a proto-lunar disk within Roche limit. They assumed that clump formation by gravitational instability and destruction by tidal force would be repeated on an orbital time scale. By estimating the energy damping rate due to inelastic collisions, they predicted the time scale of disk evolution consistent with the N -body simulations by ICS97 and KIM00. Lin & Pringle (1987) derived a similar time scale for an accreting gas disk with turbulent viscosity induced by self-gravitational instability with dimensional analysis. The time scale is much shorter than that predicted by GT78 and AT86 without self-gravity. The self-gravity would play an essential role in the evolution of a dense particle disk system.

We formalized the angular momentum transfer in a dense particle disk (in global coordinates) including both self-gravity and collisions, starting from Boltzmann equation and generalizing WT88’s formula. We performed global N -body simulations including both effects, with parameters of a protolunar disk, and evaluated angular momentum transfer rate with above formalism. We used particles up to $N = 10^5$ to represent the protolunar disk.

The protolunar disk and Saturn’s ring differ in disk mass relative to the host planet mass; the ratio is 0.01-0.05 for the former while $\sim 10^{-7}$ for the latter. The radial scale of spiral structure is given by Toomre’s critical wave length (S95; DI99), which is $\sim 2\pi(M_{\text{disk}}/M_c)r_{\text{disk}}$ (eq. [39]), where M_{disk} and r_{disk} are mass and radius of the disk and M_c is the planet

mass. Since the protolunar disk has much larger $M_{\text{disk}}/M_{\text{p}}$ than Saturnian ring, scale of spiral structure is not too small compared with the disk size, so that global calculation with $N = 10^4$ - 10^5 resolves detailed spiral structure. The angular momentum transfer in local simulations with parameters of Saturn’s ring is shown in a companion paper (Daisaka, Tanaka and Ida 2001).

We found that when $N \gtrsim$ a few thousand, the gravitational torque and collective motion regulate the angular momentum transfer. They are both determined by the surface mass density of the disk. When N is smaller, the spiral arms are less clear, and particle motion is less collective. However, angular momentum is transferred with nearly the same rate by gravitational interactions and random motion, as long as optical depth is not too small, which corresponds to $N \gtrsim$ several hundreds, for typical parameters of a protolunar disk. Therefore the result of previous works by ICS97 [$N=1,000$ - $3,000$], and KIM00 [$N=10,000$] that the Moon formation time scale after condensation of disk materials is about a month to a year is not changed in our present calculation with $N = 10^5$, although the spirals are much more clearly resolved up to fine structure in our calculation. Actually, we performed calculations with different N ($N = 10^3, 3 \times 10^3, 10^4, 3 \times 10^4, 10^5$) and confirmed that angular momentum transfer rate is almost independent of N .

Note that we must be careful to apply the above results to the evolution of a very massive disk. Since a very massive disk such as a protolunar disk evolves very rapidly, collisional heating would dominate radiative cooling, resulting in re-vaporization of particles (Thompson & Stevenson 1988). We will discuss this problem later (also see the discussions by KIM00 and Kokubo, Canup & Ida 2000). For less massive disks such as planetary rings, we need not worry about this problem.

In section 2 and 3, we show formulation of angular momentum transfer and how to calculate it from data of N -body simulations. In section 4, we explain methods and models of our numerical simulations. In section 5, we show the results of our simulations and discuss the angular momentum transfer in the protolunar disk. We compare the results to those by the local N -body simulations by WT88 and Daisaka et al. (2001). In section 6, we give conclusions and discuss the problem of vaporization due to collisional heating.

2. ANGULAR MOMENTUM TRANSFER

2.1. Boltzmann Equation

In this section, we formulate angular momentum transfer in a particulate disk, including both physical collisions and self-gravity, starting from the Boltzmann equation. The

angular momentum is carried by (i) particles' random motion (like molecular viscosity), or transferred by (ii) physical collisions and (iii) gravitational forces. During a physical collision, angular momentum is transferred by compressible waves inside the particles. When a disk is dense enough, this contribution is large (AT86). We present the formulation in particle image so that the transfer rates are easily evaluated by N -body simulations. We extend the formulation by WT88 to include the effect of gravitational torque. Borderies et al. (1985) included gravitational torque in their formulation. Although they adopted stream line approximation in which a disk is divided into fluid ringlets, their formulation may be essentially the same as the formulation presented here.

We assume that proto Earth is spherical, neglecting the deformation. Non-axisymmetric deformation may remain for a while after a giant impact, which produces extra angular momentum transfer. We will discuss the effect in section 6. We only count orbital angular momentum and neglect the spin angular momentum of particles, since the latter is usually much smaller than the former (KIM00). We thus adopt free-slip condition that tangential restitution coefficient is unity.

Number density distribution function $f(\mathbf{x}, \mathbf{v}, m)$ satisfies the Boltzmann equation, where \mathbf{x}, \mathbf{v} , and m denote position, velocity and mass of particles, respectively:

$$\frac{\partial f}{\partial t} + v_\alpha \frac{\partial f}{\partial x_\alpha} - \frac{\partial \Phi}{\partial x_\alpha} \frac{\partial f}{\partial v_\alpha} = \left(\frac{\partial f}{\partial t} \right)_c + \left(\frac{\partial f}{\partial t} \right)_g, \quad (1)$$

where the derivatives with suffix $(\partial X/\partial t)_c$ and $(\partial X/\partial t)_g$ mean the change of a quantity X is due to mutual collisions and gravitational interactions. Φ is the external potential from the central body (planet). We multiply equation (1) by m and integrating it over m . Since $\partial \Phi/\partial x_\alpha$ does not depend on m , an equation for mass density g is

$$\frac{\partial g}{\partial t} + v_\alpha \frac{\partial g}{\partial x_\alpha} - \frac{\partial \Phi}{\partial x_\alpha} \frac{\partial g}{\partial v_\alpha} = \left(\frac{\partial g}{\partial t} \right)_c + \left(\frac{\partial g}{\partial t} \right)_g, \quad (2)$$

where $g(\mathbf{x}, \mathbf{v}) \equiv \int m f dm$. In this paper, we will simulate an equal-mass (m_0) system, then $g = m_0 f$.

We integrate equation (2) in cylindrical coordinates over z, θ and \mathbf{v} . After some partial integrations, we obtain the equation of continuity:

$$\frac{\partial}{\partial t} (2\pi \Sigma) + \frac{1}{r} \frac{\partial}{\partial r} (2\pi r \Sigma u_r) = \left(\frac{\partial}{\partial t} 2\pi \Sigma \right)_c + \left(\frac{\partial}{\partial t} 2\pi \Sigma \right)_g, \quad (3)$$

where $\Sigma(r, t)$ and $\mathbf{u}(r, t)$ are surface mass density and averaged velocity defined by

$$\Sigma(r, t) \equiv \frac{1}{2\pi} \int_0^{2\pi} d\theta \int_{-\infty}^{\infty} dz \int d\mathbf{v} g, \quad (4)$$

$$\Sigma \mathbf{u}(r, t) \equiv \frac{1}{2\pi} \int_0^{2\pi} d\theta \int_{-\infty}^{\infty} dz \int d\mathbf{v} \mathbf{v} g. \quad (5)$$

Since collision and gravitational force do not change the location of particles discontinuously, the right hand side of equation (3) is 0.

Similarly, equation (2) multiplied by v_θ with integrations over z , θ and \mathbf{v} leads to the θ component of equation of motion,

$$\frac{\partial}{\partial t} (2\pi \Sigma u_\theta) + \frac{1}{r^2} \frac{\partial}{\partial r} \left(r^2 \int_0^{2\pi} d\theta \int_{-\infty}^{\infty} dz \int d\mathbf{v} v_r v_\theta g \right) = \left(\frac{\partial}{\partial t} 2\pi \Sigma u_\theta \right)_c + \left(\frac{\partial}{\partial t} 2\pi \Sigma u_\theta \right)_g. \quad (6)$$

Multiplying equation (6) by r^2 , we obtain the equation of angular momentum,

$$\frac{\partial}{\partial t} (2\pi r \Sigma r u_\theta) = -\frac{\partial F_{\text{AM}}}{\partial r}, \quad (7)$$

where

$$F_{\text{AM}} = F_{\text{trans}} + F_{\text{col}} + F_{\text{grav}} + \dot{M}_{\text{disk}} h \quad (8)$$

$$F_{\text{trans}} \equiv \int_0^{2\pi} r d\theta \int_{-\infty}^{\infty} dz \int d\mathbf{v} v_r r v_\theta g - \dot{M}_{\text{disk}} h, \quad (9)$$

$$F_{\text{col}} \equiv - \int_{r_{\text{min}}}^r dr' \left(\frac{\partial}{\partial t} 2\pi r' \Sigma r' u_\theta \right)_c, \quad (10)$$

$$F_{\text{grav}} \equiv - \int_{r_{\text{min}}}^r dr' \left(\frac{\partial}{\partial t} 2\pi r' \Sigma r' u_\theta \right)_g. \quad (11)$$

We introduced specific angular momentum $h \equiv r u_\theta$ and advective term $\dot{M}_{\text{disk}} \equiv 2\pi r \Sigma u_r$, which expresses angular momentum carried by mean radial flow. Since F_{AM} appears in equation (7) as $\partial F_{\text{AM}} / \partial r$, the minimum range of integration r_{min} is a free parameter. We choose r_{min} as the radius of inner boundary of the disk, so that F_{col} and F_{grav} are 0 inside of inner boundary and outside of outer boundary of the disk. Since $\dot{M}_{\text{disk}} = 2\pi r \Sigma u_r = \int_0^{2\pi} r d\theta \int_{-\infty}^{\infty} dz \int d\mathbf{v} u_r r u_\theta g$,

$$F_{\text{trans}} = \int_0^{2\pi} r d\theta \int_{-\infty}^{\infty} dz \int d\mathbf{v} (v_r - u_r) r (v_\theta - u_\theta) g. \quad (12)$$

This term is angular momentum transfer due to random motion of particles, analogous to that due to molecular viscosity (GT78). WT88 and AT86 called it “local” and “translational” transfer, respectively. Since we will use the term “local” in different concept, we will call this flux as “translational” angular momentum flux and use suffix “trans”. Note that in local simulation, we can set u_r to be 0 without loss of generality (WT88), but u_r is not generally

0 in global simulations. GT78 neglected self-gravity and the size of particles, so that they assumed both terms in the r.h.s. of equation (6) to be 0. In a similar sense, AT86 neglected the second term in the r.h.s of equation (6). Here both terms are nonzero and F_{col} and F_{grav} have nonzero values. Combining equation (3) and equation (7),

$$\dot{M}_{\text{disk}} \frac{\partial h}{\partial r} = -2\pi r \Sigma \frac{\partial h}{\partial t} - \frac{\partial}{\partial r} (F_{\text{trans}} + F_{\text{col}} + F_{\text{grav}}). \quad (13)$$

As long as $M_{\text{disk}} \ll M_{\text{p}}$, u_{θ} is Keplerian, $u_{\theta} = r\Omega = \sqrt{GM_c/r}$, and $\partial h/\partial t = 0$. Then

$$\dot{M}_{\text{disk}} = -\frac{1}{\frac{\partial h}{\partial r}} \frac{\partial}{\partial r} (F_{\text{trans}} + F_{\text{col}} + F_{\text{grav}}), \quad (14)$$

where $\partial h/\partial r = \Omega r/2$.

Angular momentum transfer is often expressed in terms of viscosity ν (e.g. Pringle 1981). In a viscous accretion disk,

$$\dot{M}_{\text{disk}} = -3\pi \left(\Sigma \nu + 2r \frac{\partial \Sigma \nu}{\partial r} \right), \quad (15)$$

$$F_{\text{AM}} = \dot{M}_{\text{disk}} h + 3\pi r^2 \Sigma \Omega \nu. \quad (16)$$

Comparing equations (8) and (14) with equations (15) and (16), effective viscosity ν is given by

$$3\pi \Sigma r^2 \Omega \nu = F_{\text{trans}} + F_{\text{col}} + F_{\text{grav}}. \quad (17)$$

The effective viscosities corresponding to F_{trans} , F_{col} and F_{grav} will hereafter be denoted by ν_{trans} , ν_{col} and ν_{grav} , respectively.

2.2. Bulk and Local Random Velocities

We further split F_{trans} into two parts. In an optically thick planetary ring system, collective particle motion exists associated with wake-like structure (S95; DI99). Following S95 and DI99,

$$\mathbf{v} = \mathbf{v}^{\text{bulk}} + \mathbf{v}^{\text{local}}, \quad (18)$$

where “bulk” velocity \mathbf{v}^{bulk} is locally averaged velocity (which expresses collective motion) and “local” velocity $\mathbf{v}^{\text{local}}$ is deviation from \mathbf{v}^{bulk} . S95 and DI99 showed that \mathbf{v}^{bulk} is regulated by the disk surface density but not by particle sizes. We will discuss how to separate \mathbf{v}^{bulk} and $\mathbf{v}^{\text{local}}$ in section 2.3. Note that \mathbf{v}^{bulk} is averaged over a small range only in the vicinity of the particle, while \mathbf{u} is averaged over θ from 0 to 2π .

Using equation (18), the translational angular momentum flux is divided as

$$\begin{aligned}
 F_{\text{trans}} &= \int_0^{2\pi} r d\theta \int_{-\infty}^{\infty} dz \int d\mathbf{v} (v_r^{\text{bulk}} + v_r^{\text{local}} - u_r) r (v_\theta^{\text{bulk}} + v_\theta^{\text{local}} - u_\theta) g \\
 &= \int_0^{2\pi} r d\theta \int_{-\infty}^{\infty} dz \int d\mathbf{v} (v_r^{\text{bulk}} - u_r) r (v_\theta^{\text{bulk}} - u_\theta) g \\
 &+ \int_0^{2\pi} r d\theta \int_{-\infty}^{\infty} dz \int d\mathbf{v} v_r^{\text{local}} r v_\theta^{\text{local}} g \\
 &= F_{\text{bulk}} + F_{\text{local}}.
 \end{aligned} \tag{19}$$

Since N -body simulations show that \mathbf{v}^{bulk} and $\mathbf{v}^{\text{local}}$ are not correlated, we neglected cross terms of \mathbf{v}^{bulk} and $\mathbf{v}^{\text{local}}$ as well as those of \mathbf{u} and $\mathbf{v}^{\text{local}}$.

2.3. Angular Momentum Transfer in Particle Image

In this subsection, we derive expressions of F_{local} , F_{col} and F_{grav} in a particle disk, generalizing the procedure by WT88. Particle i is represented as $\delta(\mathbf{x} - \mathbf{x}_i)\delta(\mathbf{v} - \mathbf{v}_i)\delta(m - m_i)$ in phase space $(\mathbf{x}, \mathbf{v}, m)$, where \mathbf{x}_i , \mathbf{v}_i and m_i are the position of mass, velocity and mass of particle i , and δ is delta function. Mass density distribution $g(\mathbf{x}, \mathbf{v})$ is

$$g = \int dm f = \sum_i m_i \delta(\mathbf{x} - \mathbf{x}_i) \delta(\mathbf{v} - \mathbf{v}_i). \tag{20}$$

With equation (20), we rewrite F_{local} , F_{col} and F_{grav} in particle image as below.

2.3.1. Translational Angular Momentum Flux

Substituting equation (20) into equation (12), we obtain

$$\begin{aligned}
 F_{\text{trans}}(r) &= \int_0^{2\pi} r d\theta \int_{-\infty}^{\infty} dz \int d\mathbf{v} (v_r - u_r(r)) r (v_\theta - u_\theta(r)) g \\
 &= \sum_i m_i (v_{ri} - u_r(r)) r (v_{\theta i} - u_\theta(r)) \delta(r - r_i).
 \end{aligned} \tag{21}$$

It is convenient to average F_{trans} over finite range $[r - \frac{1}{2}r_0, r + \frac{1}{2}r_0]$, where $r_p \ll r_0 \ll r$ (r_p : particle physical radius). In our numerical simulation, we adopt $r_0 = 0.02R_{\text{Roche}}$, where R_{Roche} is Roche limit radius defined by equation (44). To see the sensitivity of the result to the choice of r_0 , we also performed calculation with $r_0 = 0.05R_{\text{Roche}}$ and $r_0 = 0.1R_{\text{Roche}}$.

There is no significant difference between the cases with $r_0 = 0.02R_{\text{Roche}}$ and $r_0 = 0.05R_{\text{Roche}}$. However, in the case with $r_0 = 0.10R_{\text{Roche}}$, F_{trans} at $r = 0.4R_{\text{Roche}}$ (where r_0/r is only 1/4) differs from F_{trans} with $r_0 = 0.02R_{\text{Roche}}$ by a factor 2. Thus, r_0 should be $\lesssim 0.05R_{\text{Roche}}$. If r_0 is too small, fluctuation is large, so that we have adopt $r_0 = 0.02R_{\text{Roche}}$. Note that the other fluxes are less sensitive to the choice of r_0 .

Averaged translational angular momentum transfer is

$$\begin{aligned}\overline{F_{\text{trans}}}(r) &= \frac{1}{r_0} \int_{r-\frac{1}{2}r_0}^{r+\frac{1}{2}r_0} dr' F_{\text{trans}}(r') \\ &= \frac{1}{r_0} \sum_{r-\frac{1}{2}r_0 < r_i < r+\frac{1}{2}r_0} m_i (v_{ri} - u_{ri}) r_i (v_{\theta i} - u_{\theta i}),\end{aligned}\quad (22)$$

where \mathbf{u}_i is averaged velocity at \mathbf{r}_i .

We must define the averaged velocity \mathbf{u}_i . In a planetary ring, deviation of \mathbf{u}_i from Keplerian velocity is usually much smaller than random velocity, so that we may replace it by Kepler velocity, $(u_{ri}, u_{\theta i}) = (0, r_i \Omega(r_i))$. Then, equation (22) corresponds to the local angular momentum flux in WT88. However, since in our simulation of a protolunar disk, $|u_r|$ can not be neglected, and we do not replace \mathbf{u}_i by Kepler velocity. Substituting equation (20) into equations (4), and (5), we obtain $\Sigma(r)$ and $\mathbf{u}(r)$ in particle image. We average them over r_0 . The averaged surface density $\Sigma \equiv \overline{\Sigma}(r)$ and averaged velocity $\mathbf{u} \equiv \overline{\mathbf{u}}(r)$ are

$$\Sigma \equiv \frac{1}{2\pi r r_0} \int_{r-\frac{1}{2}r_0}^{r+\frac{1}{2}r_0} dr' \int_0^{2\pi} d\theta \int_{-\infty}^{\infty} dz \int d\mathbf{v} g = \frac{1}{2\pi r r_0} \sum_j m_j, \quad (23)$$

$$\mathbf{u} \equiv \frac{1}{2\pi r r_0 \Sigma} \int_{r-\frac{1}{2}r_0}^{r+\frac{1}{2}r_0} dr' \int_0^{2\pi} d\theta \int_{-\infty}^{\infty} dz \int d\mathbf{v} \mathbf{v} g = \frac{1}{2\pi r r_0 \Sigma} \sum_j \mathbf{v}_j m_j, \quad (24)$$

where the summations are taken over all particles in the range $[r - \frac{1}{2}r_0, r + \frac{1}{2}r_0]$.

Similarly, F_{bulk} and F_{local} in particle image are

$$\overline{F_{\text{bulk}}} = \frac{1}{r_0} \sum m_i (v_{ri}^{\text{bulk}} - u_{ri}) r_i (v_{\theta i}^{\text{bulk}} - u_{\theta i}), \quad (25)$$

$$\overline{F_{\text{local}}} = \frac{1}{r_0} \sum m_i v_{ri}^{\text{local}} r_i v_{\theta i}^{\text{local}}. \quad (26)$$

We define \mathbf{v}^{bulk} as

$$\mathbf{v}_i^{\text{bulk}} = \mathbf{u}_i + \frac{\sum_j m_j (\mathbf{v}_j - \mathbf{u}_j)}{\sum_j m_j}, \quad (27)$$

where summations are taken over the range $r_i - \frac{1}{2}\lambda_{\text{bulk}} < r < r_i + \frac{1}{2}\lambda_{\text{bulk}}$ and $\theta_i - \frac{1}{2}\lambda_{\text{bulk}}/2\pi r_i < \theta < \theta_i + \frac{1}{2}\lambda_{\text{bulk}}/2\pi r_i$. \mathbf{v}^{bulk} is mean flow velocity in the region with scale λ_{bulk} . We define n_{bulk} as a number of particles in the summation. λ_{bulk} must be so large that $n_{\text{bulk}} \gg 1$. However, λ_{bulk} should be sufficiently smaller than wave length of spiral pattern. We will use n_{bulk} rather than λ_{bulk} as a parameter. Local velocity is given by $\mathbf{v}^{\text{local}} = \mathbf{v} - \mathbf{v}^{\text{bulk}}$.

2.3.2. Collisional Angular Momentum Transfer

From equation (10),

$$F_{\text{col}} = - \int_{r_{\text{min}}}^r dr' \int_0^{2\pi} r' d\theta \int_{-\infty}^{\infty} dz \int d\mathbf{v} r' v_{\theta} \left(\frac{\partial g}{\partial t} \right)_c. \quad (28)$$

Collision term $(\partial g / \partial t)_c$ is the sum of the change of distribution function g over all collisions in a unit time. During a collision between particle A and B, the locations of the particles do not change, and the velocity of each particle changes as $\mathbf{v}_A \rightarrow \mathbf{v}_A + \Delta\mathbf{v}_A$, $\mathbf{v}_B \rightarrow \mathbf{v}_B + \Delta\mathbf{v}_B$ ($m_A \Delta\mathbf{v}_A + m_B \Delta\mathbf{v}_B = 0$). Thus, F_{col} is

$$F_{\text{col}} = - \sum_{\text{col}} \int_{r_{\text{min}}}^r dr' \{ m_A \delta(r' - r_A) \Delta v_{\theta A} + m_B \delta(r' - r_B) \Delta v_{\theta B} \} = - \sum_{\text{col}} m_A r_A \Delta v_{\theta A}, \quad (29)$$

where we assumed $r_A < r_B$ without loss of generality and used $m_A \Delta\mathbf{v}_A + m_B \Delta\mathbf{v}_B = 0$. Summation (\sum_{col}) is done for all collisions with $r_A < r < r_B$ during a unit time.

We also average F_{col} over the region $[r - \frac{1}{2}r_0, r + \frac{1}{2}r_0]$ to be consistent with $\overline{F_{\text{local}}}$ and for the summation to have enough number of collisions. Introducing $\Delta l = -m_A r_A \Delta v_{\theta A}$,

$$\overline{F_{\text{col}}} = \sum_{\text{col}} \frac{S}{r_0} \Delta l, \quad (30)$$

where summation is taken over all collisions in the region $[r - \frac{1}{2}r_0, r + \frac{1}{2}r_0]$, during a unit time, and S is radial distance by which angular momentum Δl is transferred, i.e., $r_B - r_A$. Equation (30) corresponds to nonlocal angular momentum flux in WT88. To avoid duplicate counting, $S = r_B - (r - \frac{1}{2}r_0)$ or $S = (r + \frac{1}{2}r_0) - r_A$ for the collisions which straddle the boundary $r - \frac{1}{2}r_0$ or $r + \frac{1}{2}r_0$.

2.3.3. Gravitational Angular Momentum Transfer

Substituting equation (20) into equation (11), we obtain F_{grav} in particle image as

$$\begin{aligned} F_{\text{grav}}(r) &= - \int_{r_{\text{min}}}^r dr' \int_0^{2\pi} r' d\theta \int_{-\infty}^{\infty} dz \int d\mathbf{v} r' v_{\theta} \left(\frac{\partial g}{\partial t} \right)_{\text{g}} \\ &= - \sum_{r_i < r} m_i r_i \left(\frac{\partial}{\partial t} v_{\theta, i} \right)_{\text{g}} = - \sum_{r_i < r} N_i^{\text{grav}}, \end{aligned} \quad (31)$$

where N_i^{grav} is the torque exerted on particle i by mutual gravity. Apparently, $-F_{\text{grav}}$ is total torque exerted on particles inside the radius r . Since the same amount of torque is exerted on particles outside r as recoils, F_{grav} is the angular momentum flux through a cylinder of radius r . We also average F_{grav} over the range $[r - \frac{1}{2}r_0, r + \frac{1}{2}r_0]$,

$$\overline{F_{\text{grav}}}(r) = - \sum N_i^{\text{grav}} - \sum \frac{r_i - (r - \frac{1}{2}r_0)}{r_0} N_i^{\text{grav}}, \quad (32)$$

where the first summation is taken over all particles with $r_i < r - \frac{1}{2}r_0$, and the second summation is taken over all particles in the range $[r - \frac{1}{2}r_0, r + \frac{1}{2}r_0]$.

3. ANALYTICAL ESTIMATION OF ANGULAR MOMENTUM FLUX

3.1. Estimation of Angular Momentum Flux without Wake-like Structure

In the case of a non-self gravitating particle disk, $\nu_{\text{trans}} \simeq \nu_{\text{local}}$ ($\nu_{\text{bulk}} \simeq 0$ in this case), and it is analytically derived by GT78:

$$\nu_{\text{trans}} \simeq \frac{\sigma^2}{\Omega} \left(\tau + \frac{1}{\tau} \right)^{-1}, \quad (33)$$

where σ is one dimensional random velocity and τ is optical depth defined by

$$\tau = \pi r_{\text{p}}^2 n_{\text{s}} = \frac{\pi r_{\text{p}}^2 \Sigma}{\frac{4}{3} \pi \rho_{\text{p}} r_{\text{p}}^3} = \frac{3\Sigma}{4r_{\text{p}} \rho_{\text{p}}}, \quad (34)$$

where ρ_{p} and n_{s} are particle's internal density and surface number density. A simple explanation of equation (33) is as follows. When collision frequency $\omega_{\text{c}} \gg \Omega$, radial mean free path is σ/ω_{c} . Then $\nu_{\text{trans}} \sim \sigma \cdot \sigma/\omega_{\text{c}} = \sigma^2/\omega_{\text{c}}$. When collision frequency $\omega_{\text{c}} \ll \Omega$, radial mean free path is truncated at radial excursion of epicycle motion, σ/Ω . Since only a fraction of

particles actually transfers angular momentum during one epicycle, ω_c/Ω must be multiplied. Then, $\nu_{\text{local}} \sim \sigma(\sigma/\Omega)(\omega_c/\Omega) \sim \sigma^2\omega_c/\Omega^2$. Replacing ω_c by $\tau\Omega$ (GT78),

$$\nu_{\text{trans}} \sim \begin{cases} \frac{\sigma^2}{\Omega} \frac{1}{\tau} & \text{for } \tau \gg 1 \\ \frac{\sigma^2}{\Omega} \tau, & \text{for } \tau \ll 1 \end{cases}. \quad (35)$$

Interpolation of equation (35) gives equation (33). Greenberg (1988) gives a more detailed description.

AT86 introduced the effect of particle size in their analytical estimation, and found that at high optical depth $\nu_{\text{col}} > \nu_{\text{trans}}$. Their result is consistent with numerical simulations by WT88. Their result can be fitted as (Schmit & Tscharnuter 1995)

$$\nu = \nu_{\text{col}} + \nu_{\text{trans}} = C \frac{\sigma^2}{\Omega} \tau^\alpha, \quad (36)$$

where $C = 0.78$ and $\alpha = 1.26$.

These formulae are derived with assumption that the spatial distribution of particles is uniform and distribution in velocity space is stationary Gaussian distribution. When wake-like structure develops in a self-gravitational disk, particles are distributed no longer uniformly, and spatially nearby particles move collectively with velocity ellipsoid like rotating bar structure (DI99). With the excitation of bulk motion, ν_{trans} should be much enhanced.

3.2. Estimation of Angular Momentum Flux with Wake-like Structure

Gravitational angular momentum transfer in a disk with spiral pattern is analytically given by Lynden-Bell & Kalnajs (1972), under WKB approximation. The outward angular momentum flux by self-gravitational torque is (Appendix A)

$$F_{\text{grav}} = \frac{\pi}{2} G r^2 \lambda_r H^2 \sin i \cos^2 i. \quad (37)$$

where i , H , and λ_r are pitch angle, density amplitude, and radial wave length of spirals (Larson 1984). In the linear theory, the wave length is (e.g. Binney & Tremaine 1987)

$$\lambda_{\text{cr}} = \frac{2\pi^2 G \Sigma}{\Omega^2}. \quad (38)$$

Note that

$$\lambda_{\text{cr}} = 2\pi \frac{\pi \Sigma r^2}{M_c} r \sim 2\pi \frac{M_{\text{disk}}}{M_c} r, \quad (39)$$

which is consistent with the results of our N -body simulations (Fig. 3). In our simulations, $H \sim \Sigma$ when $\tau \sim O(1)$, and i is from 15 to 45 degree (section 5.2). Here we simply put $\sin i \cos^2 i \sim O(1)$. Though derivation of equation (37) uses the assumption that the spiral is tightly winding ($\lambda_r \ll r$), the assumption is often good approximation even for relatively loosely winding spirals with $\lambda_r \sim r/2$ (e.g. Binney & Tremaine 1987). Thus, F_{grav} and the corresponding viscosity are

$$F_{\text{grav}}^{\text{est}} \sim \frac{\pi^3 G^2}{\Omega^2} r^2 \Sigma^3, \quad (40)$$

$$\nu_{\text{grav}}^{\text{est}} \sim \frac{1}{3} \frac{\pi^2 G^2}{\Omega^3} \Sigma^2. \quad (41)$$

A similar formula can be derived by the results of Borderies et al. (1985), if the results of N -body simulations are used. In their model, gravitational interactions between stream lines are calculated. The stream lines are perturbed by external potential and have the form $r(r, \phi) = a\{1 - e(a) \cos m[\phi + \Delta(a)]\}$, where a and m are unperturbed semi-major axis and the azimuthal mode of perturbation potential. With negative $d\Delta/da$, these streamlines form trailing density spiral. Borderies et al. (1985) showed that in the tightly winding limit, angular momentum transfer due to gravitational torque is

$$F_{\text{grav}}^{\text{est}} \sim \pi^2 G \Sigma^2 a^3 m e^2. \quad (42)$$

N -body simulations show that when spiral structure develops, $v_r^{\text{bulk}} \gg v_r^{\text{local}}$ and $v_r \sim v_r^{\text{bulk}} \sim 2\pi G \Sigma / \Omega$ (S95; DI99; equation (57) below), which means $e \sim 2\pi G \Sigma / \Omega^2 a$. With this empirical relation and $m \sim (2\pi a / \lambda_{\text{cr}}) \tan i$, equation (42) reads as

$$F_{\text{grav}}^{\text{est}} \sim 4\pi^3 \frac{G^2}{\Omega^2} a^2 \Sigma^3. \quad (43)$$

This is similar to equation (40).

4. NUMERICAL METHODS AND MODEL

We numerically simulated the evolution of protolunar disks by N -body simulations, including physical collisions and self-gravity. We performed several sets of simulations with different initial surface density distribution. For each set, we performed 5 runs with different particle numbers. We started the calculation from an impact-debris disk whose mass is mostly within Roche limit. For simplicity, we considered no heat generation and vaporization here. We followed collisions and gravitational interactions step by step and calculated F_{trans} , F_{col} and F_{grav} , defined as equations (22), (30) and (32) at different time. We also calculated

F_{bulk} and F_{local} , given by equations (25) and (26). The sampling time was about 100^{-1} Kepler time, and we averaged them over 2 Kepler time.

We set material density of the proto Earth ρ_{\oplus} as 5.5 g cm^{-3} and that of disk particles ρ_{p} as 3.3 g cm^{-3} , which are the present Earth’s and lunar bulk densities, respectively. With these densities, Roche limit radius is

$$R_{\text{Roche}} = 2.456 \left(\frac{\rho_{\text{p}}}{\rho_{\oplus}} \right)^{-1/3} R_{\oplus} = 2.9 R_{\oplus}, \quad (44)$$

where R_{\oplus} is radius of the Earth. We adopt the proto Earth mass as the present Earth mass $M_{\oplus} = 5.97 \times 10^{27} \text{ g}$. In this case, Kepler time T_{K} at $r = R_{\text{Roche}}$ is about 7 hr.

We use T_{K} , M_{\oplus} and R_{Roche} as units of time, mass and distance. The physical radius of a particle with mass m is

$$r_{\text{p}} = \left(\frac{m}{M_{\oplus}} \right)^{1/3} \left(\frac{\rho_{\text{p}}}{\rho_{\oplus}} \right)^{-1/3} R_{\oplus} = \frac{1}{2.456} \left(\frac{m}{M_{\oplus}} \right)^{1/3} R_{\text{Roche}}. \quad (45)$$

4.1. Integration Method

We follow the orbits of all particles numerically integrating the equation of motion,

$$\frac{d\mathbf{v}_i}{dt} = -GM_{\oplus} \frac{\mathbf{x}_i}{|\mathbf{x}_i|^3} - \sum_{j \neq i}^N Gm_j \frac{\mathbf{x}_i - \mathbf{x}_j}{|\mathbf{x}_i - \mathbf{x}_j|^3}. \quad (46)$$

We use fourth ordered Hermite scheme with individual time step scheme. Full description of the scheme is given in Makino & Aarseth (1992). Let d be distance between mass centers of two particles. When we detect d smaller than the sum of particle radii ($r_{\text{p1}} + r_{\text{p2}}$), we change velocities according to the restitution coefficient. For detailed adjustment of collision and rebounding to avoid numerical difficulty, we follow Richardson (1994).

Since particle number is limited in N-body simulation, fragmentation can not be included in practice. As shown below, typical random velocity of particles is $\sim \pi G \Sigma / \Omega$, which ranges from a few hundreds ms^{-1} to a few kms^{-1} . The corresponding specific energy is from 2×10^8 to $2 \times 10^{10} \text{ ergg}^{-1}$. A collision with such energy may results in a catastrophic disruption (e.g. Benz & Asphaug 1999) unless particles are small enough that material strength is important. However, the angular momentum transfer depends on surface density, but not on each particle size, as shown below. The disruption would not affect the angular momentum transfer process. If a disruptive collision is supposed to occur, we represent energy dissipation during the disruption as an effective restitution coefficient for inelastic collision. Since we

do not know the value of the effective restitution coefficient, we perform runs with different values.

We assume that tangential restitution coefficient $\varepsilon_t = 1$, neglecting the exchange between orbital angular momentum and spin angular momentum (KIM00). For simplicity, we use normal restitution coefficient ε_n that is independent of collision velocity. The mean reduction of relative velocity due to the inelasticity is (Canup & Esposito 1995)

$$1 - \varepsilon = 1 - \left[\frac{\varepsilon_n^2 v_n^2 + \varepsilon_t^2 v_t^2}{v_n^2 + v_t^2} \right]^{1/2}. \quad (47)$$

Assuming mean tangential and normal collision velocities, v_t and v_n , are similar, effective restitution coefficient ε is about 0.7, for example, if $\varepsilon_n = 0.1$. This corresponds to that about half ($\sim 0.7^2$) the fraction of relative kinetic energy of collision is given to fragments. In nominal cases, we adopt $\varepsilon_n = 0.1$, which may be rather dissipative one. We also study the effect of the restitution coefficient with additional set of simulations with different ε_n from 0.1 to 0.8. We will show that angular momentum transfer rates are almost independent of ε_n except for highly elastic ε_n ($\varepsilon_n \gtrsim 0.6$); in the highly elastic cases, velocity distribution is so high that spiral arms are not developed.

If the relative velocity after a collision is sufficiently small, the collision results in gravitationally bounded particles. At $r \gtrsim R_{\text{Roche}}$, the particles are gravitationally bounded if Jacobi energy is negative and particles are within Hill sphere (Ohtsuki 1993; Canup & Esposito 1995; Kokubo et al. 2000). We adopt rubble pile model, in which no mergers are allowed. In this case, gravitationally bounded particles form particle aggregates. When the aggregates are scattered to inside of Roche limit, particle size overflows Hill sphere and tidal force disrupts the aggregates (Ohtsuki 1993; Canup & Esposito 1995; Kokubo et al. 2000).

4.2. Parameters and Initial Conditions

We simulate disks with equal-mass particles. The initial surface density Σ is distributed as $\Sigma \propto a^\alpha$ in the range $a_{\text{min}} < a < a_{\text{max}}$, where a is semimajor axis. The initial conditions of the disks are shown in Table I. We set a_{max} near Roche limit, so that most particles are initially within Roche limit. SET 1-4 start from centrally condensed disks with $\alpha = -3$, with different total disk masses. Runs with constant surface density ($\alpha = 0$) are investigated in SET 5 in comparison. We simulated the disks by runs with $N = 10^3, 3 \times 10^3, 10^4, 3 \times 10^4$ and 10^5 for each SET. Totally we performed 25 runs with $\varepsilon_n = 0.1$. We call a run with $j \times 1000$ particles in SET k as “RUN k - j K”. We also performed additional simulations (SET 6), with fixed initial particle number $N = 3 \times 10^4$, changing the normal restitution coefficient

as $\varepsilon_n = 0.2, 0.4, 0.6$ and 0.8 . For each ε_n , we perform 4 runs with different initial surface density distribution similar to SET 1-4 (SET6 includes 16 runs).

Orbital eccentricities and inclinations are given by Rayleigh distribution with given mean values $\langle e^2 \rangle^{1/2}$ and $\langle i^2 \rangle^{1/2}$. Specific choice of initial $\langle e^2 \rangle^{1/2}$ and $\langle i^2 \rangle^{1/2}$ does not affect the results because they approach quasi-equilibrium values only on one or two Kepler times.

5. RESULTS

5.1. Overall Disk Evolution

We simulated the evolution of a protolunar disk and investigated angular momentum transfer, which causes mass redistribution of the disk. First we show overall evolution of the disk. In Figs. 1 (a)-(f), we show snapshots of disk evolution for SET 2 with 1×10^5 particles (RUN 2-100K). We also show snapshots in r - z plane in Figs. 2 (a)-(f). At $t = 0$ (panel a), particles are distributed azimuthally uniformly. In SET 2, we give initially high random velocity, so that the disk scale height is large (Fig. 2(a)) to avoid self-gravitational instability initially. Inelastic collisions quickly damp the random motion. Since the orbital rotation time is shorter and optical depth is higher in inner region, the damping is faster there. At $t = 2T_K$ (panel b), the spirals begin to develop in the inner region. However, as we will discuss later, clear spiral structure does not develop in the innermost region. At $t = 6T_K$ (panel c) and $t = 10T_K$ (panel d), spirals extend to the outer region, and disk material is transferred beyond the Roche limit. At $t = 20T_K$ (panel e), lunar seeds (large aggregates) are formed beyond the Roche limit. At $t = 30T_K$ (panel f), two large lunar seeds further grow. The largest and the second largest seeds consist of about 5000 and 2400 particles respectively in this stage. These lunar seeds grow to a single moon. This is typical evolution of the protolunar disk (ICS97; KIM00).

In Figs. 3 (a)-(e), we show snapshots of RUN 1-100K, 2-100K, 3-100K, 4-100K, with different M_{disk} from about $1.5M_L$ to $5M_L$. The radial wave length of spirals is larger in heavier disks as predicted by equation (38). Equation (38) agrees well with numerical results, as shown in section 5.2.

We show time evolution of surface density distributions of RUN 2-100K and RUN 5-30K in Figs. 4 (a) and (b). In RUN 5-30K surface density is initially flat. After several Kepler times, quasi-equilibrium state is achieved in both cases, and disk mass is rather steadily transferred. In the outer region, mass is transferred outward to form lunar seeds, which correspond to a small peak of surface density beyond Roche limit. In the inner part, particles fall onto the Earth in compensation, and surface density decreases.

As we will show in the following sections, effective viscosity is proportional to $r_p^{1/2}\Sigma^{3/2}$ in the region $r \lesssim 0.6R_{\text{Roche}}$ (section 5.3.1), and to Σ^3 in the region $r \gtrsim 0.6R_{\text{Roche}}$ (section 5.3.2). Collisional angular momentum transfer is dominant at $r \lesssim 0.6R_{\text{Roche}}$, while other two processes are dominant at $r \gtrsim 0.6R_{\text{Roche}}$. In Figs. 4 (c) and (d), we show the surface density distribution at $t = 6T_K$ and $t = 18T_K$ of SET 2 with various N . In the inner region, the peak height of surface density is lower for smaller N , because $\nu \propto r_p^{1/2}\Sigma^{3/2}$ increases with decrease in N . On the other hand, the surface density distribution in the outer region is almost independent of N , because effective viscosity is independent of physical size r_p . In this region, angular momentum transfer is regulated by collective effects, so that ν is dependent only on Σ , and does not depend on r_p . The lunar accretion processes are regulated by mass and angular momentum transfer near R_{Roche} as explained in ICS97 and KIM00. Figs. 4 (c) and (d) indicate they are almost independent of r_p or particle number N of N-body simulation.

We show magnified snapshots of SET 2 in Figs. 5 (a) and (b) and SET 3 in Figs. 5 (c) and (d). Figs. 5 (a) and (c) are $N = 1 \times 10^5$ cases and (b) and (d) are $N = 1 \times 10^4$ cases. Spiral structure with high density contrast develops only in the outer region. To clarify quantitative features of spiral structure, we adopt autocorrelation analysis.

5.2. Autocorrelation Analysis for spiral structure

We calculated autocorrelation directly by superposing the relative locations of particles, following S95 and DI99 with a little modification. The autocorrelation of spatial distribution function n is

$$\text{Corr}(\Delta r, \Delta\theta, r) = \frac{1}{f_n} \int_{r-\frac{1}{2}r_0}^{r+\frac{1}{2}r_0} dr' \int_0^{2\pi} r' d\theta n(r' + \Delta r, \theta + \Delta\theta) n(r', \theta), \quad (48)$$

where Δr , $\Delta\theta$ and f_n are relative locations and normalizing factor. As shown below, Corr is a function of r . Substituting $n(r, \theta) = \sum m_i \delta(r - r_i) \delta(\theta - \theta_i) / r$ to equation (48),

$$\begin{aligned} \text{Corr}(\Delta r, \Delta\theta, r) &= \frac{1}{f_n} \sum_i \sum_j m_i m_j \int_{r-\frac{1}{2}r_0}^{r+\frac{1}{2}r_0} dr' \frac{\delta(r' + \Delta r - r_i) \delta(r' - r_j)}{r' + \Delta r} \\ &\quad \times \int_{r-\frac{1}{2}r_0}^{r+\frac{1}{2}r_0} d\theta \delta(\theta + \Delta\theta - \theta_i) \delta(\theta - \theta_j) \\ &= \frac{1}{f_n} \sum_i \sum_j \frac{m_i m_j}{r_i} \delta(\Delta r - (r_i - r_j)) \delta(\Delta\theta - (\theta_i - \theta_j)), \end{aligned} \quad (49)$$

where j is summed over particles in the region $[r - \frac{1}{2}r_0, r + \frac{1}{2}r_0]$ for each reference radius r , while summation over i is taken for all particles. Equation (49) is superposition of particles' relative distribution. We used 60×200 mesh in $(\Delta r, \Delta \theta)$ space in the region $\Delta r = [-0.3, 0.3]$, and $\Delta \theta = [-1, 1]$ (radian) and averaged Corr in each mesh. Since radial density gradient is large, we choose following normalizing factor,

$$f_n = 2\pi \int_{r-\frac{1}{2}r_0}^{r+\frac{1}{2}r_0} dr' r' \Sigma(r' + \Delta r) \Sigma(r'). \quad (50)$$

With above normalizing factor, Corr is 1 everywhere if surface density is a function only of r .

Since unstable wave length depends on Σ , Corr depends on surface density. In global simulation, Σ changes with time, so that we choose snapshot data from different runs with similar surface density and averaged them. We choose only snapshot with initial $N \geq 3 \times 10^4$ and $\varepsilon_n \leq 0.2$. We show the contour maps of Corr in Figs. 6. We averaged 10 to 30 Corr snapshots data to draw each figure. The straight dotted lines represent pitch angles with 15, 30 and 45 degrees. We show Corr at $r = 0.7R_{\text{Roche}}$ with different surface density in panel (a) $\Sigma = 0.005\text{-}0.006$, (b) $\Sigma = 0.008\text{-}0.010$ and (c) $\Sigma = 0.012\text{-}0.016$. Pitch angle is always ~ 20 degrees and it does not depend on surface density within the range of our simulation. However, we found that pitch angle increases with r . Similar tendency is also shown in local simulations (S95 and DI99). Panel (d), (e), and (f) show Corr at $r = 0.5R_{\text{Roche}}$, $0.6R_{\text{Roche}}$ and $0.9R_{\text{Roche}}$, with $\Sigma = 0.012\text{-}0.016$, $0.012\text{-}0.016$, and $0.004\text{-}0.005$. In innermost region (d), there is no clear structure as shown in Figs. 5, and Corr is almost featureless. In outer region ((e) and (f)), clear bar like structure appears at the center. The pitch angle is about 15 degree at $r = 0.6R_{\text{Roche}}$ and about 45 degree at $r = 0.9R_{\text{Roche}}$. In the analytical estimate in the following sections, we adopt 30 degrees as an averaged pitch angle.

In panel (a) or (b), we also recognize the bars next to the central bars. The radial separation increases with Σ . The corresponding λ_{cr} (eq. [38]) for panel (a), (b) and (c) are $0.046R_{\text{Roche}}$, $0.061R_{\text{Roche}}$ and $0.095R_{\text{Roche}}$. Our numerical result and linear theory agree well.

5.3. Angular Momentum Transfer

Figs.7 (a), (b), (c) and (d) show angular momentum fluxes F_{col} , F_{grav} and F_{trans} in RUN 2-100K, RUN2-10K, RUN 3-100K and RUN 3-10K, after spiral patterns fully develop but before large lunar seeds grow, which may perturb the entire disk. The horizontal axis is distance from the center of the Earth, and vertical axis is angular momentum flux. In inner

region ($r \lesssim 0.6R_{\text{Roche}}$), collisional angular momentum flux F_{col} dominates. In outer region ($0.6R_{\text{Roche}} \lesssim r$), $F_{\text{grav}} \sim F_{\text{trans}} > F_{\text{col}}$. The difference should reflect the fact that spiral structure develops in the outer region while it does not in the inner region.

Before discussing angular momentum fluxes in each region in detail, we consider the condition for development of spiral structure. In the linear theory, axisymmetric density perturbations grow if $Q < 1$ where Q is defined by $\sigma\Omega/\pi G\Sigma$ (Toomre 1964) with velocity dispersion σ . We show Q values as a function of r averaged over from $t = 8T_K$ to $t = 10T_K$ for SET 2, and from $t = 4T_K$ to $t = 6T_K$ for SET 3 in Figs.8. In outer region, velocity of collective motion is pumped up by spirals and Q is greater than 1. Local simulations show that $Q \sim 2$ when spirals develop (S95; DI99). In our simulation, Q increases with r , up to about 5 at $r = R_{\text{Roche}}$, which may be caused by global effects. In the inner region where optical depth is high, Q is enhanced by incompressibility of the particles. Physical meaning of Q is $\sim \Omega^2/\pi G\rho$, where spatial density $\rho \sim \Sigma/h$ and disk scale height $h \sim \sigma/\Omega$ are used. In the high optical depth case, ρ is limited by particle material density ρ_p and Q should be $\gtrsim \Omega^2/\pi G\rho_p$. The minimum value of Q is independent of σ and r_p (or N), and increases with decrease in r . Ward & Cameron (1978) argued that mid-plane pressure stabilizes the disk and predicted that gravitational instability does not occur when $r \lesssim 0.5R_{\text{Roche}}$ even if random velocity is small. A similar criterion is also derived by comparing particle's Hill radius with physical size (DI99). Our result that spiral structure does not develop in the inner region is consistent with these predictions.

5.3.1. Angular Momentum Transfer in Inner Region

In Fig. 9, we plot $\nu_{\text{col}}/r_p^2\Omega$ obtained by our simulations at $r = 0.5R_{\text{Roche}}$, at various times of all RUNs with various Σ and r_p . Collisional viscosity ν_{col} is well fitted as

$$\nu_{\text{col}} \simeq 1.35\Omega r_p^2 \tau^{1.5}. \quad (51)$$

We found ν_{col} is consistent with the results of AT86. In the inner region, one dimensional velocity dispersion $\sigma \sim r_p\Omega$ (S95). Thus, equation (36) reads as

$$\nu = \nu_{\text{col}} + \nu_{\text{local}} \sim 0.78\Omega r_p^2 \tau^{5/4}. \quad (52)$$

In Fig. 9, we also plot $(\nu - \nu_{\text{local}})/r_p^2\Omega$ (solid line), where we use equation (33) for ν_{local} . The results of our N-body simulation agree with equation (52) except for a numerical factor ~ 2 -3. ν_{col} also agrees with the result of local simulations when the spiral structure does not develop (Daisaka et al. 2001).

Since $\tau \propto \Sigma r_p^{-1}$ (eq.[34]), $\nu_{\text{col}} \propto r_p^{1/2} \Sigma^{3/2}$. For the same Σ , ν_{col} decreases with decrease in r_p , that is, increase in N . From equations (17) and (51),

$$F_{\text{col}} = 3\pi \Sigma r^2 \Omega \nu_{\text{col}} \simeq 8.26 r^2 \Omega^2 \Sigma^{5/2} \rho^{-3/2} r_p^{1/2}. \quad (53)$$

Eliminating r_p using equation (34), F_{col} at $r = 0.5$ is

$$F_{\text{col}} \simeq C_c \tau^{-1/2} \left(\frac{\pi^3 G^2}{\Omega^2} r^2 \Sigma^3 \right), \quad (54)$$

where $C_c \simeq 1.2$.

5.3.2. Angular Momentum Transfer In Outer Region

5.3.2.1 Angular Momentum Transfer by Gravitational Torque

In the outer region, where spiral structure develops, F_{grav} and F_{trans} overwhelm F_{col} . We show F_{grav} as a function of surface density at $r = 0.7R_{\text{Roche}}$ in Fig. 10 (a). We plot the results of all RUNs in SET 1-4, during $t = 6T_K$ to $t = 16T_K$ with sampling intervals $2T_K$. Since Σ is different between different RUNs and between different times, we obtain F_{grav} with various Σ at the same r . The analytical estimation of $F_{\text{grav}}^{\text{est}} = (\pi^3 G^2 / \Omega^2) r^2 \Omega^3 \sin i \cos^2 i$ (eq.[40]) with $i = 30$ degrees is represented by a dashed line. Angular momentum flux F_{grav} in numerical results is in agreement with $F_{\text{grav}}^{\text{est}}$, in particular in the case of high τ where spiral structure clearly appears.

We introduce numerical factor C_g , which is defined as

$$F_{\text{grav}} = C_g \frac{\pi^3 G^2}{\Omega^2} r^2 \Sigma^3. \quad (55)$$

The estimation $F_{\text{grav}}^{\text{est}}$ for $i = 30$ degree corresponds to $C_g = 0.38$. We plot C_g at $r = 0.7R_{\text{Roche}}$ in numerical results in Fig. 10 (b). When $\tau \gtrsim 0.1$, C_g is ~ 1 -2, independent of τ and r_p , which indicates F_{grav} has the same functional form as $F_{\text{grav}}^{\text{est}}$.

5.3.2.2 Translational Angular Momentum Transfer

We show the relation between F_{trans} and Σ at $r = 0.7r_{\text{Roche}}$ in Fig. 11 (a). The dashed line is explained below. In a similar way to equation (55), we define a numerical factor C_t as

$$F_{\text{trans}} = C_t \frac{\pi^3 G^2}{\Omega^2} r^2 \Sigma^3. \quad (56)$$

We show C_t in Fig 11 (b). Figs. 11 show F_{trans} is always almost equal to F_{grav} at $0.7R_{\text{Roche}}$ where spiral structure develops. In the outermost region near Roche limit, the results are more noisy in global simulation. However, C_g and C_t seem to be larger by a factor of 2-3 near Roche limit in general. F_{col} becomes less important with increase of r (see Figs. 7). The local N -body simulation (Daisaka et al. 2001) also shows similar tendency on r .

In the outer region, F_{trans} is far greater than that corresponding to equation (33) with $\sigma \sim r_p \Omega$, which was derived under assumption of spatial uniformity by GT78. The development of spiral structure is responsible for the enhancement of F_{trans} . To see this more clearly, we separate F_{trans} into the component of bulk motion F_{bulk} and that of random motion F_{local} , as explained in section 2.3.2.

In Figs. 12, we show F_{bulk} and F_{local} of RUNs in SET 3, averaged from $t = 4T_k$ to $6T_k$, as a function of n_{bulk} . The dashed lines are λ_{bulk} , which is the scale of the region in which n_{bulk} particles exist. Figs. 12 (a) and (b) show F_{bulk} and F_{local} at $r = 0.7R_{\text{Roche}}$ for RUN 3-100K, RUN3-10K, respectively. The predicted radial scale of spirals λ_{cr} (eq.[38]) in the cases of Figs. 12 (a) and (b) are about $0.08R_{\text{Roche}}$. In Fig. 12 (a), F_{bulk} and F_{local} are almost constant up to $n_{\text{bulk}} \sim 100$, and $\lambda_{\text{bulk}} \sim \lambda_{\text{cr}}$. This means that the particles move collectively as a group with scale $\sim \lambda_{\text{cr}}$ in which about 100 particles exist. In this scale, $F_{\text{local}} \ll F_{\text{bulk}}$, and translational angular momentum transfer is almost wholly due to this bulk motion. This is the case also for RUN 2-10K (Fig. 12(b)). In this case, particles move collectively with about 10 neighboring particles with the scale $\lambda_{\text{bulk}} \sim \lambda_{\text{cr}}$. These results explain why F_{trans} is enhanced over equation (33) and has the functional dependence predicted by equation (56).

When the structure develops, $Q = \sigma \Omega / \pi G \Sigma \sim O(1)$. Since $F_{\text{bulk}} \gg F_{\text{local}}$, $\sigma \sim v^{\text{bulk}} \gg v^{\text{local}}$. Then,

$$v^{\text{bulk}} \sim \frac{\pi G \Sigma}{\Omega} Q \sim \frac{\pi G \Sigma}{\Omega}. \quad (57)$$

Since particles move as groups, these groups may be treated as super particles with random velocity v_{bulk} . Life time of each structure is $\sim \Omega^{-1}$, so that collision frequency of the super particles is $\omega_c \sim \Omega$. Thus, translational viscosity and corresponding angular momentum flux may be

$$\nu_{\text{trans}}^{\text{est}} \sim \frac{(v_r^{\text{bulk}})^2}{\Omega} \sim \frac{\pi^2 G^2 \Sigma^2}{\Omega^3}, \quad (58)$$

$$F_{\text{trans}}^{\text{est}} \sim 3 \frac{\pi^3 G^2}{\Omega^2} r^2 \Sigma^3. \quad (59)$$

Note that $F_{\text{trans}}^{\text{est}} \sim F_{\text{grav}}^{\text{est}}$ and $\nu_{\text{trans}}^{\text{est}} \sim \nu_{\text{grav}}^{\text{est}}$. We also plot $F_{\text{trans}}^{\text{est}}$ in Fig. 11 (a) with a dashed line. Considering a disk with turbulence induced by self-gravitational instability, Ward & Cameron (1978) and Lin & Pringle (1987) derived a similar angular momentum transfer rate.

In parameters of Saturn’s ring, Daisaka et al. (2001) studied more detailed relation between angular momentum fluxes and τ , Σ , and r by local simulations.

5.3.3. Angular momentum transfer in higher restitution coefficient case

We have studied the cases with $\varepsilon_n = 0.1$. This choice may lead to rather high cooling rate of random velocity, keeping Q value low. Equilibrium random velocity is determined by heating due to transfer of shear motion to random motion through collisions and damping due to inelastic collisions (GT78; Ohtsuki 1993). However, for $\varepsilon_n > 0.67$, the damping is no longer strong enough to attain equilibrium state and random velocity keeps growing (GT78). Then, Q value should be so high that the spiral structure does not appear. To examine the effect of higher ε_n , we performed additional simulations (SET6) with restitution coefficient 0.2, 0.4, 0.6 and 0.8. We show the snapshots of some cases in SET6 in Figs. 13. Initial surface density distribution is the same as that in SET3. Panel (a) is the case with $\varepsilon_n = 0.4$ at $t = 8T_K$. Panel (b) is the case with $\varepsilon_n = 0.6$. For $\varepsilon_n \lesssim 0.4$, spiral structure seems similar to the runs with $\varepsilon_n = 0.1$. However, when $\varepsilon_n = 0.6$, the spiral is less clear. In the case with $\varepsilon_n = 0.8$, any structure does not appear. We show angular momentum transfer rates in Figs. 14. These rates are averaged over $t = 6T_K$ to $t = 8T_K$. For $\varepsilon_n = 0.6$, gravitational transfer is less dominant. This reflects the less clear spiral structure (Fig. 14 (b)).

We show F_{grav} as a function of Σ for different ε_n in Figs. 15 (a). Only data with optical depth larger than 0.3 is chosen. Dashed lines are the best fitted lines with assumption that $F_{\text{grav}} \propto \Sigma^3$. While F_{grav} decreases with increase of ε_n , the relation $F_{\text{grav}} \propto \Sigma^3$ remains. F_{trans} and F_{col} are plotted in panels (b) and (c). Although they decrease with increase of ε_n , the decrease is smaller than that in F_{grav} . (F_{trans} does not show clear dependence as Σ^3 in large ε_n case. We omit the fitted line in the case with $\varepsilon_n = 0.8$ because of large dispersion.)

Panel (d) shows the corresponding C_g , C_t and C_c as a function of ε_n . Error bars represent standard deviations. In general, as ε_n increases, angular momentum transfer, in particular F_{grav} , decreases. However, the results do not change so much (C_g , C_c and C_t change only by factor 2) except for highly elastic case $\varepsilon_n \gtrsim 0.6$, when the spiral structure is not clear.

5.3.4. Summary of Angular Momentum Transfer

In an optically thick particle disk, angular momentum is transferred in different ways in inner and outer regions. The boundary between inner and outer regions is about 0.6-0.7 R_{Roche} . In the inner region, clear spiral structure does not develop, so that the analytical

formulae assuming spatial uniformity work well (e.g. GT78; AT86). In this region, collisional angular momentum transfer dominates, which is well fitted by equation (51).

In the outer region, F_{grav} and F_{trans} are enhanced by the spiral structure and dominate F_{col} . They are both proportional to Σ^3 and independent of r_p . In outer region, $F_{\text{grav}} \simeq F_{\text{trans}} > F_{\text{col}}$. Defining $C_i (i = \text{g, t, c})$ as F_{grav} , F_{trans} and $F_{\text{col}} = C_i (\pi^2 G^2 / \Omega^2) r^2 \Sigma^3 (i = \text{g, t, c})$, our numerical results show $C_{\text{total}} = C_{\text{g}} + C_{\text{t}} + C_{\text{c}} \sim C_{\text{g}} + C_{\text{t}} \sim 4-8$. In local simulations, $C_{\text{total}} \sim 2$ in the region corresponding to $r \sim 0.7R_{\text{Roche}}$ and $C_{\text{total}} \sim 6$ at $r \sim 0.9R_{\text{Roche}}$ (Daisaka et al. 2001). The numerical factor slightly increases with r in local simulations (Daisaka et al. 2001). Similar tendency is found in our global simulations. As the restitution coefficient increases, numerical factors decrease and relative importance of F_{grav} diminishes. However, the transfer rate changes only by a factor 2 unless ε_n is highly elastic ($\varepsilon_n \gtrsim 0.6$).

We show time evolution of surface density distribution in log scale in Figs. 16, for (a) RUN 3-100K and (b) RUN 5-30K. Initial surface density distribution is proportional to $\Sigma \propto r^{-3}$ in RUN 3-100K and flat in RUN 5-30K. Dashed lines in the figures are proportional to $\Sigma^{-3/2}$. Surface density distribution after initial relaxation but before formation of lunar seeds in our simulations is consistent with $\Sigma \propto r^{-3/2}$ in outer region. The relation $\Sigma \propto r^{-3/2}$ is the steady accretion solution ($d\dot{M}_{\text{disk}}/dr = 0$) to equation (15) with constant C_{total} (Lin & Pringle 1987).

6. CONCLUSIONS AND DISCUSSION

We have investigated angular momentum transfer and associated mass transfer in a particle disk where physical collisions as well as self-gravity are important. First we presented formulation of angular momentum transfer in the disk, starting from Boltzmann equation. Next, we performed global N-body simulation with $N = 10^3-10^5$ to directly calculate angular momentum transfer fluxes, based on the above formulation. We simulated disks that correspond to a protolunar disk generated by a giant impact on the proto Earth. The disk has total mass $\sim 0.02 - 0.06M_c$ where M_c is the central body mass and most mass is initially within the Roche limit of the central body. In such a dense disk, spiral structure is formed by self-gravity and energy dissipation due to inelastic collisions, except for innermost region where tidal force of the central body is too strong.

In the region $0.6R_{\text{Roche}} \lesssim r \lesssim 1R_{\text{Roche}}$, angular momentum transfer is regulated by gravitational torque exerted by spiral structure and collective motion of particles in the spirals. ICS97 and KIM00 showed that formation of the Moon is regulated by angular momentum transfer in this region. With increasing τ , spiral structure becomes clearer.

When $\tau \gtrsim 0.2$, angular transfer rate is

$$F_{\text{grav}} + F_{\text{trans}} + F_{\text{col}} \sim F_{\text{grav}} + F_{\text{trans}} = (C_g + C_t) \frac{\pi^3 G^2}{\Omega^2} r^2 \Sigma^3, \quad (60)$$

where $C_g + C_t$ is about 4-8 in the parameters for a protolunar disk. Then, surface density distribution approaches to distribution in steady accretion that is proportional to $r^{-3/2}$.

The average optical depth is

$$\tau = \frac{N \pi r_p^2}{\pi (R_{\text{Roche}}^2 - R_{\oplus}^2)} = \left(\frac{3M_{\text{disk}}}{4\pi\rho} \right)^{2/3} \frac{1}{(R_{\text{Roche}}^2 - R_{\oplus}^2)} N^{1/3}. \quad (61)$$

Since $C_g + C_t$ saturates for $\tau \gtrsim 0.2$, particle number N in global simulation must be

$$N \gtrsim 3500 \left(\frac{M_{\text{disk}}}{3M_L} \right)^{-2}. \quad (62)$$

The relation between the initial disk mass and the mass of the Moon was derived by ICS97. When initial mass is distributed within Roche limit, required initial disk mass is about 3 times the present lunar mass. Thus, evolution of the protolunar disk can be followed with rather small number of particles; $N \gtrsim 3000$ is enough and $N \gtrsim 1000$ ($\tau \gtrsim 0.15$) may be okay.

In the innermost region, spiral structure does not develop and angular momentum transfer is dominated by collisions between particles, and the corresponding viscosity has positive dependency on particle size. N-body simulations with limited number overestimate the diffusion process in this region. However, this does not change the lunar formation, since lunar seed is formed by the angular momentum transfer in outer region. Once a large proto-moon is formed, the remaining disk would interact with the lunar seed, and the disk materials would eventually be scattered to fall to the Earth (ICS97; KIM00). Thus, we conclude that N-body simulation of evolution of a protolunar disk is not affected by limited number of particles, as long as $N \gtrsim 1000$ -3000.

The time scale of viscous evolution is given as $\sim \Delta r^2/\nu$. Since total viscosity is

$$\nu_{\text{total}} = C_{\text{total}} \frac{\pi^2 G^2}{3\Omega^3} \Sigma^2, \quad (63)$$

the time scale of disk evolution is

$$t_{\text{ev}} \simeq \frac{500}{C_{\text{total}}} \left(\frac{\Sigma}{0.01M_{\oplus}R_{\text{Roche}}^{-2}} \right)^{-2} \left(\frac{\Delta r}{R_{\text{Roche}}} \right)^2 \left(\frac{r}{R_{\text{Roche}}} \right)^{-9/2} T_{\text{K}}. \quad (64)$$

Since $C_{\text{total}} \simeq C_g + C_t$ is about 4-8, $t_{\text{ev}} \sim 100T_K$, which is consistent with lunar formation time obtained by ICS97 and KIM00. The development of spiral structure is essential for the rapid evolution of a protolunar disk.

We comment on the physical processes we neglected and validity of assumptions in our simulations. One process we neglected is fragmentation. Since typical random velocity is large, catastrophic disruption would occur in particle collisions. Thus, realistic particle size would be much smaller. However as long as random energy damping is sufficient, spiral structure develops as well. Thus fragmentation would not affect the evolution of the disk, since the angular momentum transfer in the outer region has no dependency on particle size, being regulated by the movement of particles as a group.

We simply assumed that all particles have the same size, so that filling factor is 0.7 at most. If size distribution is included, the effective material density increases. It may expand the region where clear spiral develops to more inner region. Also, random velocity of smaller particles would be larger if size distribution is included. However, size distribution does not prevent the spiral structure developing in the simulations in (ICS97 and KIM00), so that this would not affect the physics in principle.

We also assumed that the central body is spherical. Objects interact with tidal bulges raised on the Earth, so that materials exterior to the synchronous orbit migrate outward, and interior materials migrate inward. The time scale of tidal evolution of a body with one lunar mass is of order of 10^3 yr (Canup & Esposito 1996). This is much longer than the time scale of disk evolution and the tidal effect is not essential for disk evolution. The formed moon would migrate outward sweeping up remnants of the disk (Canup, Levison, & Stewart 1999). The Earth itself may be deformed considerably without tidal bulges. In SPH simulations of giant impact, the core of impactor penetrates through the mantle material and accumulates on proto-Earth, and forms a rotating quadrupole (e.g. Cameron 1997). Though the quadrupole subsides substantially in a day or two, some fraction of quadrupole component may remain. This would not effect the angular momentum transfer due to local instability, which was discussed in this paper, since the time scale of angular momentum transfer by local instability is very short. However, this may have considerable effect in a longer time scale.

We also assumed that a protolunar disk is an entirely particulate disk. In recent SPH simulations (Cameron 1997) suggests that vapor/liquid and solid phase coexist in a protolunar disk after the giant impact, with average temperature above 4000K. Assuming that an initial disk with 3 lunar mass is within Roche limit, heat dissipation required for the disk evolution is about 1.5×10^{37} erg, which is about a half of latent heat of vaporization of silicate of the disk mass. If an entire disk is evaporated, Toomre's Q value is

$\sim 3(T/1000\text{K})^{1/2}(r/R_{\text{Roche}})^{-3/2}[\Sigma/(0.01M_{\oplus}/R_{\text{Roche}}^2)]^{-1}$, with mean molecular weight 30, and the disk would be stable against gravitational instability. During a short time scale of dynamical disk evolution, it is difficult for radiation to cool down the disk (Thompson & Stevenson 1988). If gravitational instability is aborted by the vaporization, the disk evolution would be regulated by the cooling time of the disk (Thompson & Stevenson 1988). The disk evolution and Moon accretion would depend on how the disk with vapor/liquid-solid mixture evolves, as discussed in KIM00. If the disk remains within Roche limit until the disk is sufficiently cooled down to develop gravitational instability, a single moon would be formed just beyond Roche limit. The disk would be condensed from outer region. Spirals would develop in the condensed region, which results in rapid diffusion of the materials there. A single moon accretes the materials diffused out, staying at the location just beyond Roche limit. The eventual mass of the moon would be the same as the results of N-body simulations neglecting vaporization, because final moon mass is determined by redistribution of disk angular momentum to the moon and materials that fall to the Earth (ICS97; KIM00), although time scale may be regulated by cooling.

The heat generation problem occurs in a very heavy disk such as a protolunar disk. The result that angular momentum transfer in a particulate disk within Roche limit is regulated by gravitational instability is applicable to other disk systems, such as planetary rings or small satellite formation. In planetary rings, the only difference is that the wave length of structure λ_{cr} is much smaller since $M_{\text{disk}}/M_c \ll 1$ (see eq. [39]). Daisaka et al. (2001) performed the local N-body simulations with the parameters of Saturn’s B-ring, and calculated the angular momentum transfer rate in a similar way. They found that the angular momentum transfer in Saturn’s B-ring is also regulated by wake like structure and equation (60) also holds.

We are grateful for helpful comments by Hidekazu Tanaka on formalizations. Discussion with Hiroshi Daisaka was valuable. We also thank his technical comments on numerical calculations. The numerical calculations were carried out on a special purpose computer GRAPE-4. We thank Junichro Makino and Eiichro Kokubo for technical advice on GRAPE-4. We also thank the anonymous referee for useful comments. This work was supported by Grant-in-Aid for Scientific Research (c) 12640405.

A. ANGULAR MOMENTUM FLUX DUE TO GRAVITATIONAL TORQUE

A formula for angular momentum flux due to gravitational torque with a spiral pattern is given by Lynden-Bell & Kalnajs (1972). From the definition (eq. [11]),

$$F_{\text{grav}} = \int_{r_{\text{min}}}^r dr' \int_0^{2\pi} r' d\theta \int_{-\infty}^{\infty} dz \rho \frac{\partial \Phi'}{\partial \theta}, \quad (\text{A1})$$

where Φ' is potential due to disk material. Combining equation (A1) with Poisson equation, it is expressed as

$$F_{\text{grav}}(r) = \frac{1}{4\pi G} \int_0^{2\pi} r d\theta \int_{-\infty}^{\infty} dz \frac{\partial \Phi'}{\partial r} \frac{\partial \Phi'}{\partial \theta}. \quad (\text{A2})$$

We represent surface density distribution as

$$\Sigma(r, \theta, t) = \Sigma_0(r, t) + \Sigma_1(r, \theta, t) = \Sigma_0(r, t) + H(r, t)e^{m\theta + f_s(r, t)}, \quad (\text{A3})$$

where Σ_0 is azimuthally averaged density distribution and $f_s(r, t)$ is shape function for the n th arm satisfying

$$n\Phi' + f_s(r, t) = \text{constant (mod } 2\pi). \quad (\text{A4})$$

Using tightly winding approximation (e.g. Binney & Tremaine 1987), the potential due to Σ_1 is given by

$$\Phi'_1(r, \theta, z, t) = -\frac{2\pi G}{|k|} H(r, t) \text{Re} \left\{ e^{i\{m\theta + f_s(r, t)\} - |kz|} \right\}, \quad (\text{A5})$$

where k is wave number. Note that r component of k is $k_r = \partial f_s / \partial r = k \cos i$. Substituting equation (A5) into equation (A2), and using $m = k_r r \tan i$, where i is pitch angle, we obtain

$$F_{\text{grav}} = \frac{\pi^2 G r k_r}{k^2} \frac{k_r}{k} m H^2 = \frac{\pi}{2} G r^2 \lambda_r \sin i \cos^2 i, \quad (\text{A6})$$

where $\lambda_r = 2\pi/k_r$.

REFERENCES

- Araki, S. & Tremaine, S. 1986, *Icarus* 65,83
- Benz, W., & Asphaug, E., 1999, *Icarus*, 142, 5
- Binney, J., & Tremaine, S. 1987, *Galactic dynamics* (Princeton, NJ, Princeton University Press)
- Borderies, N., Goldreich, P., & Tremaine, S. 1983, *Icarus*, 55, 124

- Borderies, N., Goldreich, P., & Tremaine, S. 1985, *Icarus*, 63, 406
- Cameron, A. G. W. & Ward, W. R. 1976, *Lunar Sci. Abs.*, 7, 120
- Cameron, A. G. W. 1997, *Icarus*, 126,126
- Canup, R. M., Esposito, L. W. 1995, *Icarus*, 113, 331
- Canup, R. M., Esposito, L. W. 1996, *Icarus*, 119, 427
- Canup, R. M., Levison, H. F., & Stewart, G. R. 1999, *AJ*, 117, 603
- Daisaka, H. & Ida, S. 1999, *Earth and Planet and Space*, 51, 1195-1213
- Daisaka, H., Tanaka, H., & Ida, S. 2001, submitted to *Icarus*
- Goldreich, P., & Tremaine, S. 1978, *Icarus*, 34, 227
- Greenberg, R. 1988, *Icarus*, 75, 527
- Hartmann, W. K. & Davis, D. R. 1975, *Icarus*, 24, 504
- Ida, S., Canup, R. M., & Stewart, G. R. 1997, *Nature*, 389, 353
- Kokubo, E., Ida, S., & Makino J. 2000, *Icarus*, 148, 419
- Kokubo, E., Canup, R. M., & Ida S. 2000, in *The Origin of Earth and Moon*, ed. Canup, R. M. and Righter, K. (Univ. of Arizona Press), 145
- Larson, R.B. 1984 *MNRAS*, 206, 197
- Lin, D.N.C., & Pringle, J.E. 1987 *MNRAS*, 225, 607
- Lynden-Bell, D., & Kalnajs, A. J. 1972, *MNRAS*, 157, 1
- Lynden-bell, D., and Pringle, J.E. 1974, *MNRAS*, 168, 603
- Makino, J., & Aarseth, S.J. 1992, *PASJ*, 44, 141
- Ohtsuki, K. 1993, *Icarus*, 106, 228
- Petit, J.-M. & Greenberg, R. 1996, *Icarus*, 123, 524
- Pringle, J.E. 1981, *ARA&A*, 19, 137
- Richardson, D. C. 1994, *MNRAS*, 269, 493

Salo, H. 1995, *Icarus*, 117,287

Schmit, U., & Tscharnuter, W. M. 1995, *Icarus*, 115, 304

Thompson, C., & Stevenson, D.J. 1988, *ApJ*, 333, 452

Toomre, A. 1964, *ApJ*, 139, 1217

Ward W.R., & Cameron A.G.W. 1978, *Proc. Lunar Planet. Sci. Conf.*, Abs. IX, 1205

Wisdom, J., & Tremaine, S. 1988, *AJ*, 95, 925

Fig. 1.— Snapshots of RUN 2-100K. (a), (b), (c), (d), (e) and (f) are snapshots at $t = 0, 2, 6, 10, 20, 30T_K$, respectively. The inner circle is the Earth with radius $0.343R_{\text{Roche}}$. The large outer circle shows the Roche limit.

Fig. 2.— Snapshots of RUN 2-100K on r - z plane, corresponding to Figures 1. Three circles show Earth’s radius, $0.5 R_{\text{Roche}}$, and $1R_{\text{Roche}}$.

Fig. 3.— Snapshots of (a) RUN 1-100K, (b) 2-100K, and (c) 3-100K at $t = 6T_K$ and (d) 4-100K at $t = 4T_K$.

Fig. 4.— Time evolution of surface density in (a) RUN 2-100K and (b) RUN 5-30K. Surface density profile at (c) $t = 6T_K$ and (d) $t = 18T_K$ in SET 2. The Earth’s radius is at $0.343 R_{\text{Roche}}$.

Fig. 5.— Magnified snapshots for (a) RUN 2-100K and (b) RUN 2-10K at $t = 10T_K$, (c) RUN 3-100K and (d) RUN 3-10K at $t = 6T_K$. The three circles are the radius of Earth, $0.5R_{\text{Roche}}$ and $1R_{\text{Roche}}$.

Fig. 6.— Contours of autocorrelation $\text{Corr}(\Delta r, \Delta\theta)$ at $r = 0.7R_{\text{Roche}}$, with different surface density, (a) $\Sigma = 0.005$ - 0.006 , (b) $\Sigma = 0.008$ - 0.010 , and (c) $\Sigma = 0.012$ - 0.016 . Panel (d), (e), and (f) are the results with (d) $r = 0.5R_{\text{Roche}}$ and $\Sigma = 0.012$ - 0.016 , (e) $r = 0.6R_{\text{Roche}}$ and $\Sigma = 0.012$ - 0.016 , and (f) $r = 0.9R_{\text{Roche}}$ and $\Sigma = 0.004$ - 0.005 .

Fig. 7.— Angular momentum fluxes F_{col} , F_{grav} and F_{trans} as functions of r , averaged over $t = 4$ - $6T_K$. (a) RUN 2-100K, (b) RUN 2-10K, (c) RUN 3-100K, and (d) RUN 3-10K.

Fig. 8.— Q value as a function of r , in (a) SET 2 and (b) SET 3 at $t = 6T_K$.

Fig. 9.— Collisional viscosity $\nu_{\text{col}}/\Omega r_p^2$ is given as a function of τ , in the region where spiral structure does not develop. Circles are the results of N -body simulations at $r = 0.5R_{\text{Roche}}$ for different times and RUNs. A dashed line is a fitted value given by equation (51). The solid line is analytical estimate by GT78 and AT86.

Fig. 10.— (a) F_{grav} as a function of surface density Σ at $r = 0.7R_{\text{Roche}}$. The dashed line shows the estimated F_{grav} which is given as equation (40) with $i = 30$ degree. (b) C_g as a function of optical depth τ at $r = 0.7R_{\text{Roche}}$.

Fig. 11.— (a) F_{trans} as a function of surface density Σ at $r = 0.7R_{\text{Roche}}$. The dashed line is $F_{\text{trans}}^{\text{est}}$ (eq. [59]). (b) C_t as a function of optical depth τ at $r = 0.7R_{\text{Roche}}$.

Fig. 12.— F_{bulk} and F_{local} as a function of n_{bulk} at $r = 0.7R_{\text{Roche}}$ in (a) RUN 3-100K and (b) RUN 3-10K. Filled circles are F_{bulk} and circles are F_{local} . Dashed lines are λ_{bulk} corresponding

to n_{bulk} .

Fig. 13.— Snapshots for SET 6, with (a) $\varepsilon_n = 0.4$ and (b) $\varepsilon_n = 0.6$. Initial surface density is similar to SET 3.

Fig. 14.— Angular momentum fluxes F_{col} , F_{grav} and F_{trans} as functions of r , with different ε_n . (a) $\varepsilon = 0.4$ and (b) $\varepsilon = 0.6$.

Fig. 15.— Angular momentum fluxes F_{col} , F_{grav} and F_{trans} as function of Σ , with different ε_n . Dashed lines are best fitted line assumed that fluxes are proportional to Σ^3 . (a) F_{grav} , (b) F_{trans} , and (c) F_{col} . Dashed line in panel (b) is fitted for $\varepsilon_n = 0.1$. (d) is relation between ε_n and corresponding C_g and C_c .

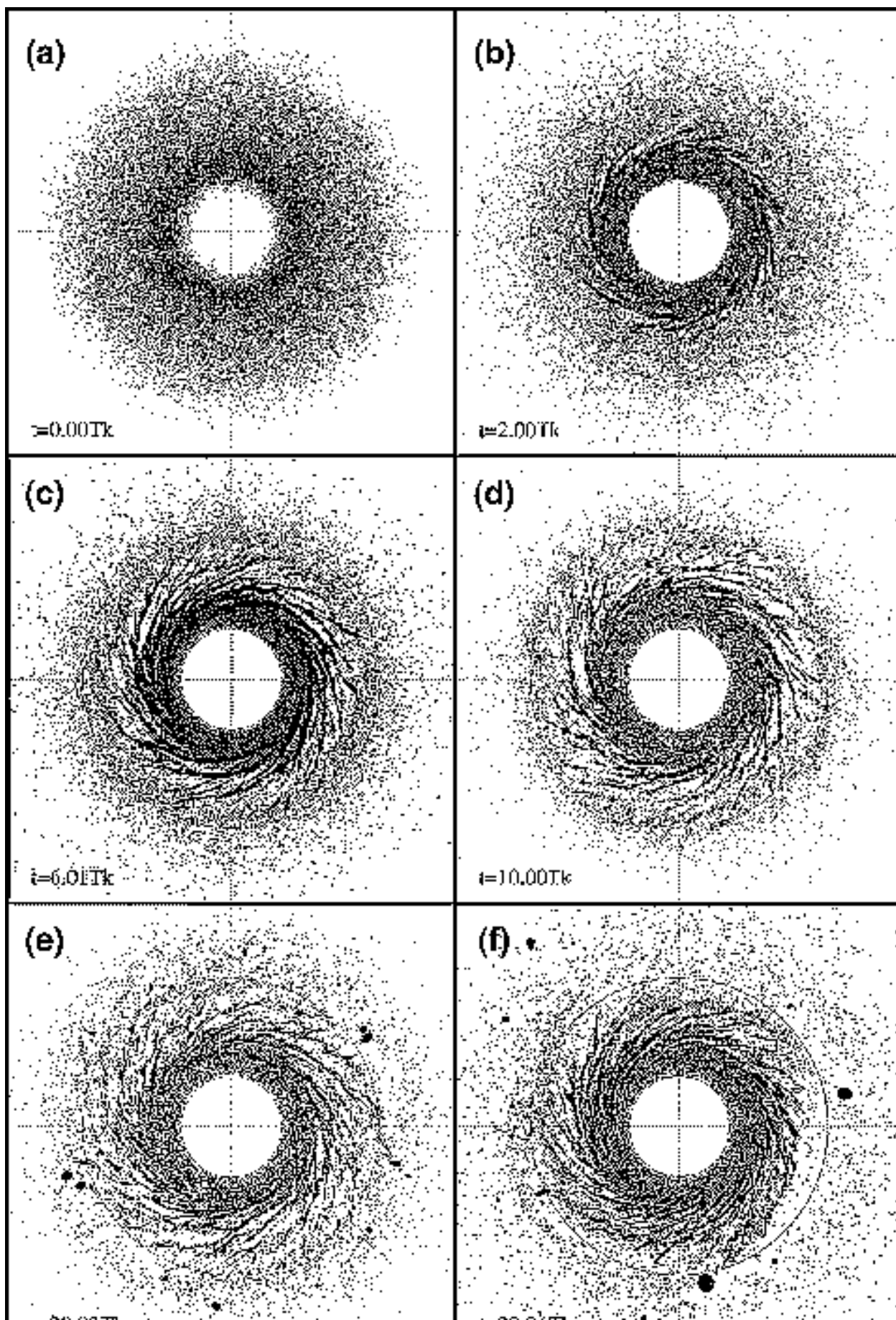
Fig. 16.— Time evolution of surface density Σ in (a) RUN 3-100K and (b) RUN 5-30K. Dashed lines are proportional to $r^{-3/2}$.

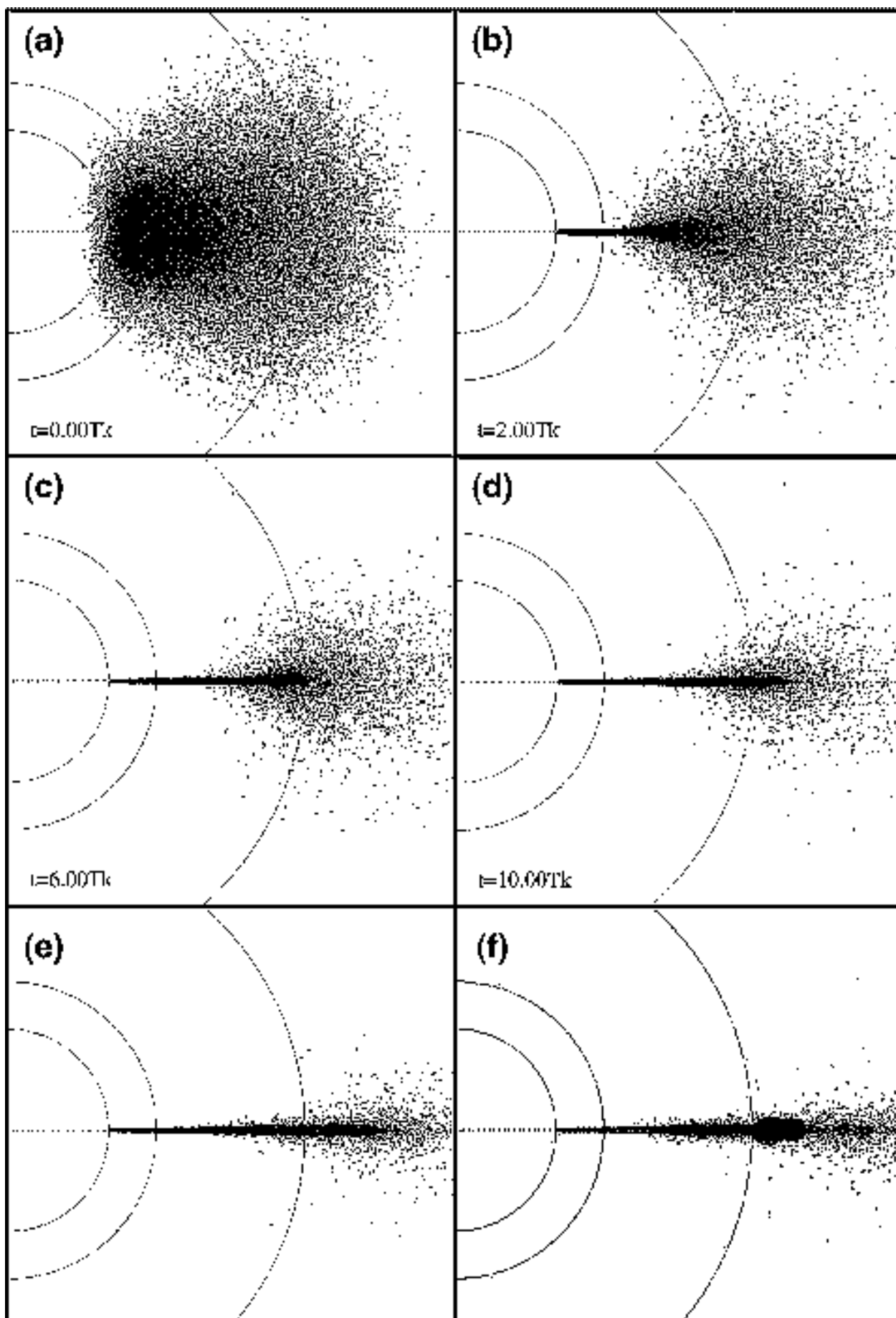
Table 1. Parameters of initial disks for SET 1-6

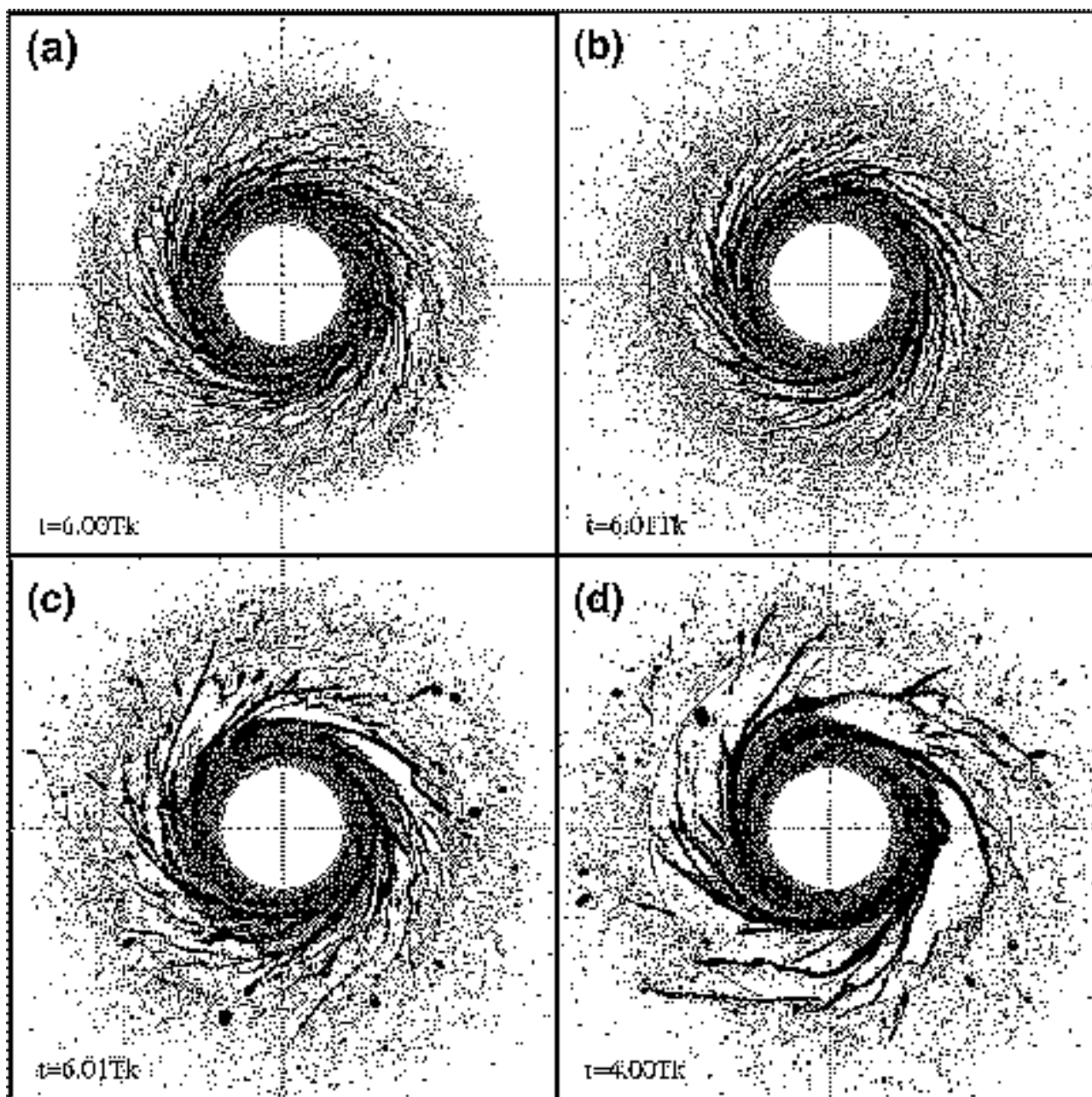
SET	Disk Mass (M_L) ^a	α	a_{\min} (R_{Roche})	a_{\max} (R_{Roche})	$\langle e^2 \rangle^{1/2}$	$\langle i^2 \rangle^{1/2}$
SET1	1.67	-3	0.4	1.2	0.05	0.05
SET2	2.47	-3	0.4	1.1	0.15	0.3
SET3	3.20	-3	0.4	1.1	0.05	0.05
SET4	4.94	-3	0.4	1.1	0.05	0.05
SET5	3.20	0	0.4	1.1	0.05	0.05
SET6	... ^b	-3	0.4	1.1	0.05	0.05

^a $M_L = 0.0125M_{\oplus} = 7.35 \times 10^{25}\text{g}$

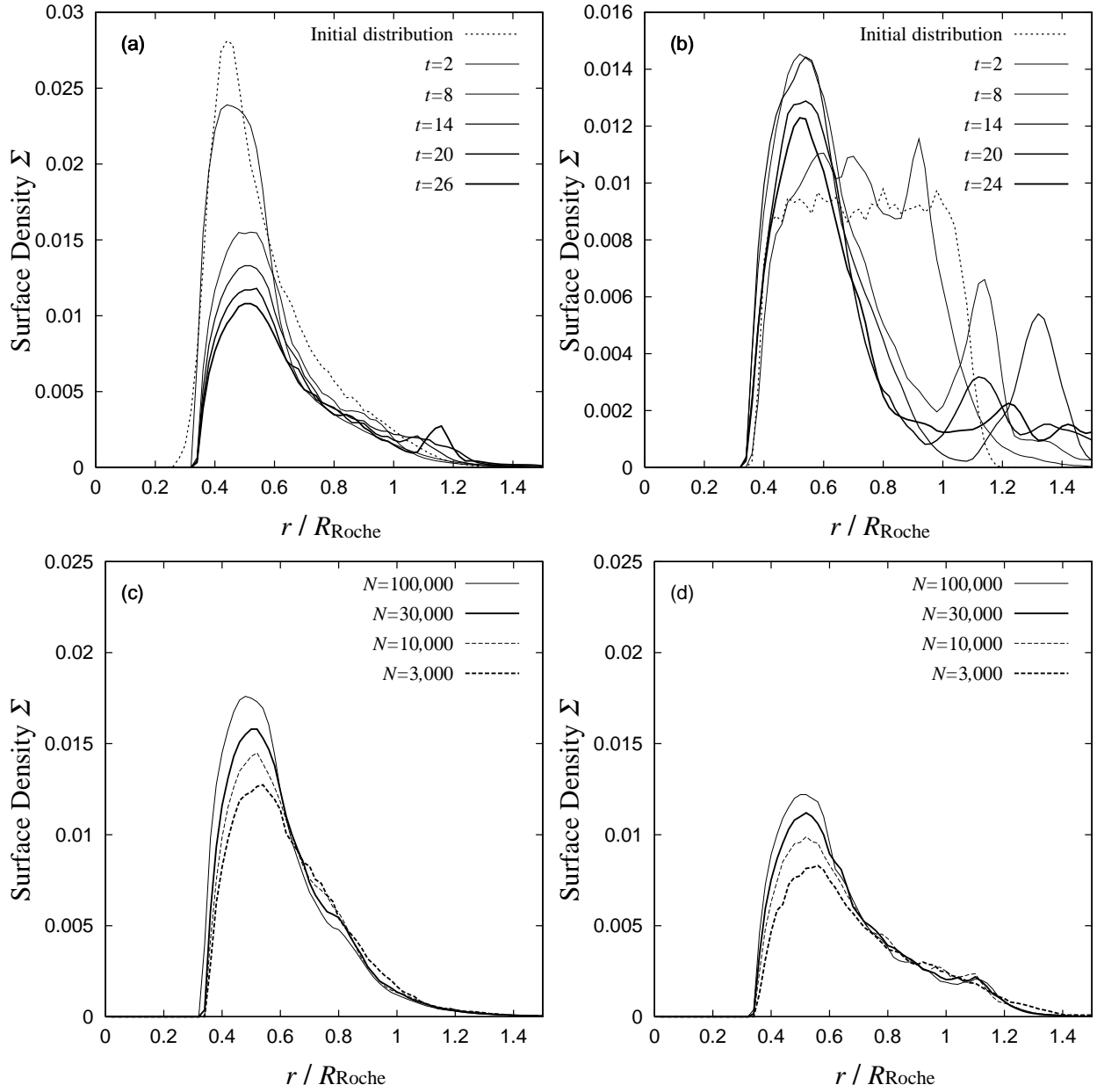
^bFor each $\varepsilon_n = 0.2, 0.4, 0.6$ and 0.8 , we performed four RUNs with disk mass 1.67, 2.47, 3.20 and 4.94.



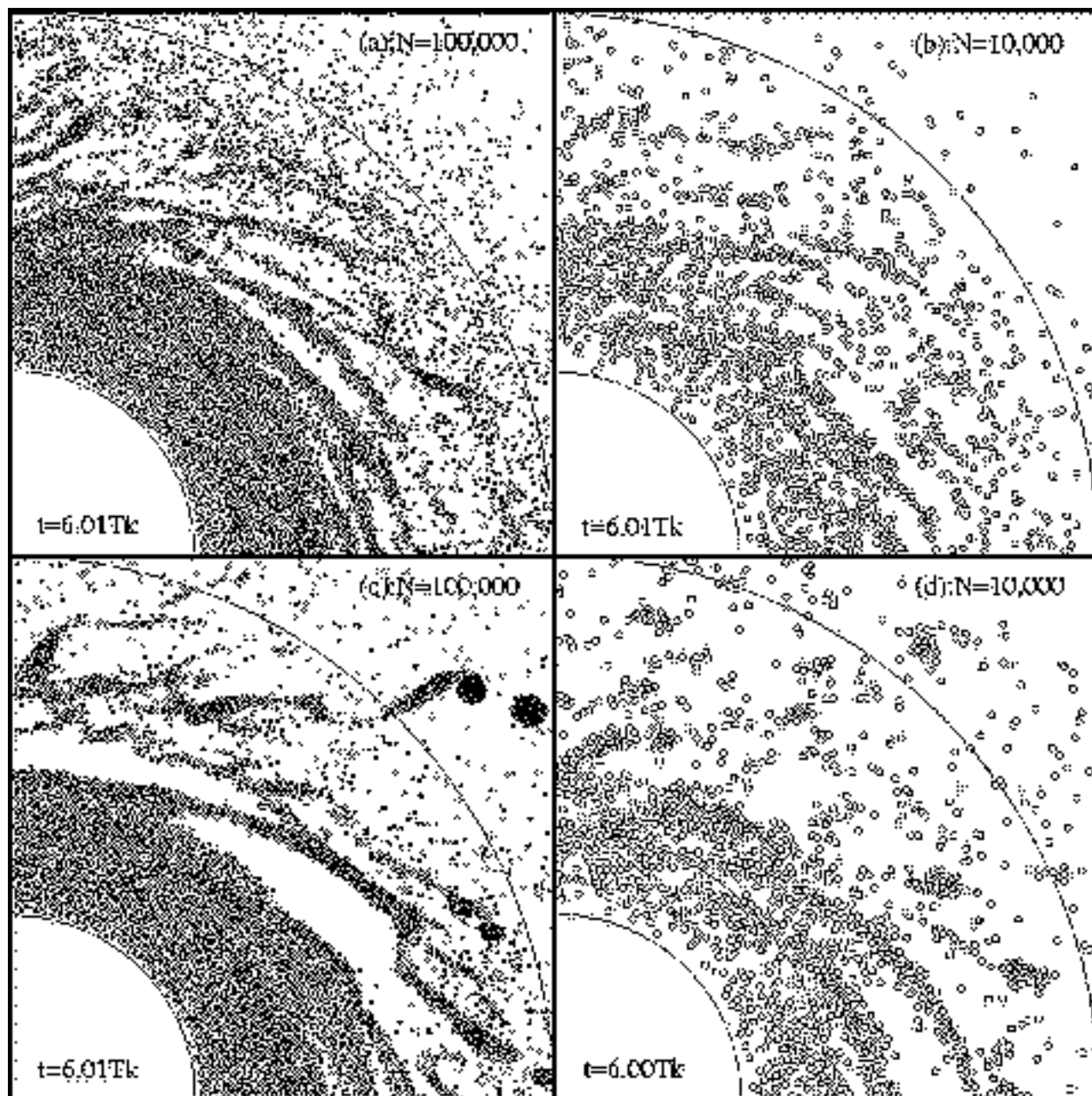




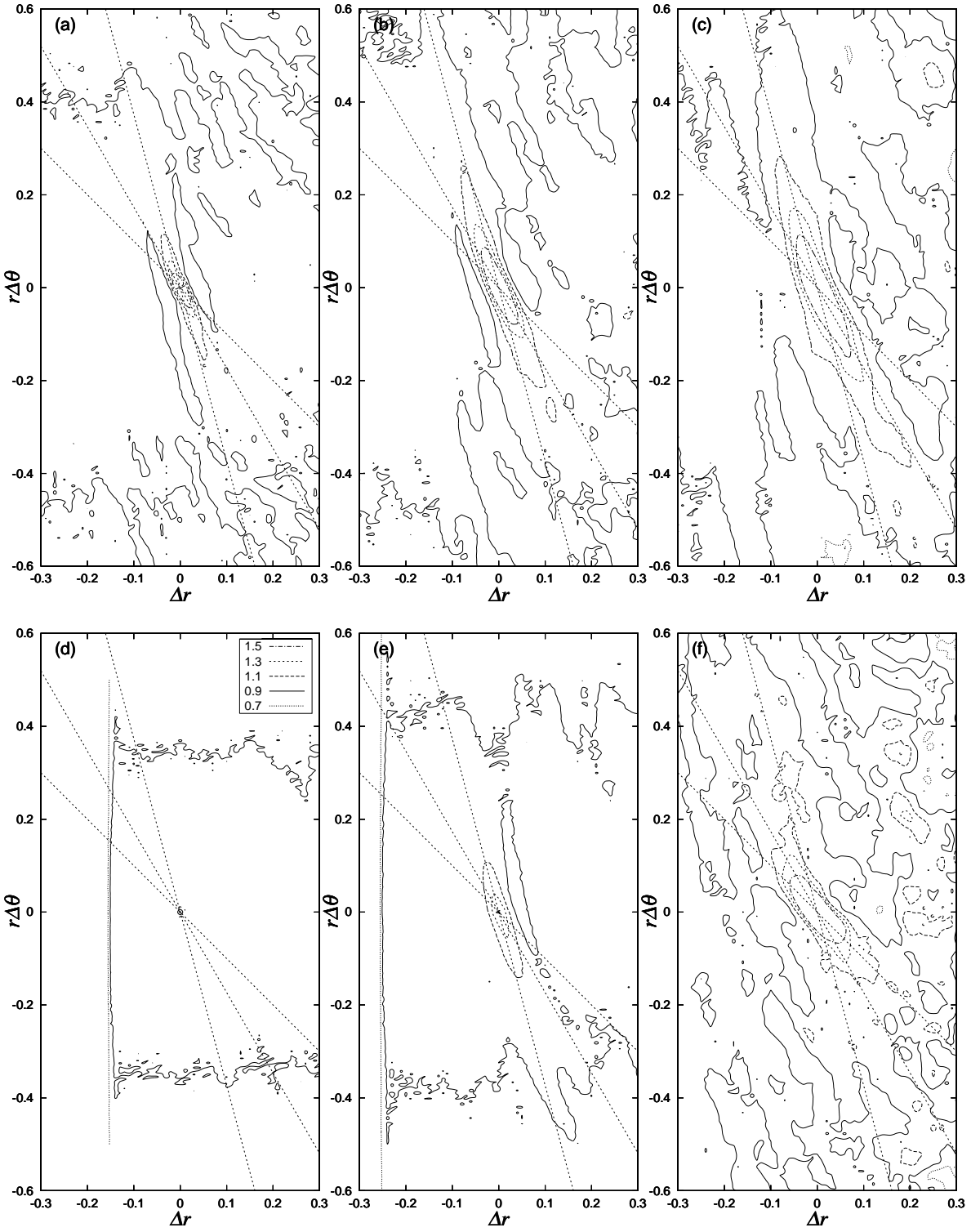
Figs. 3



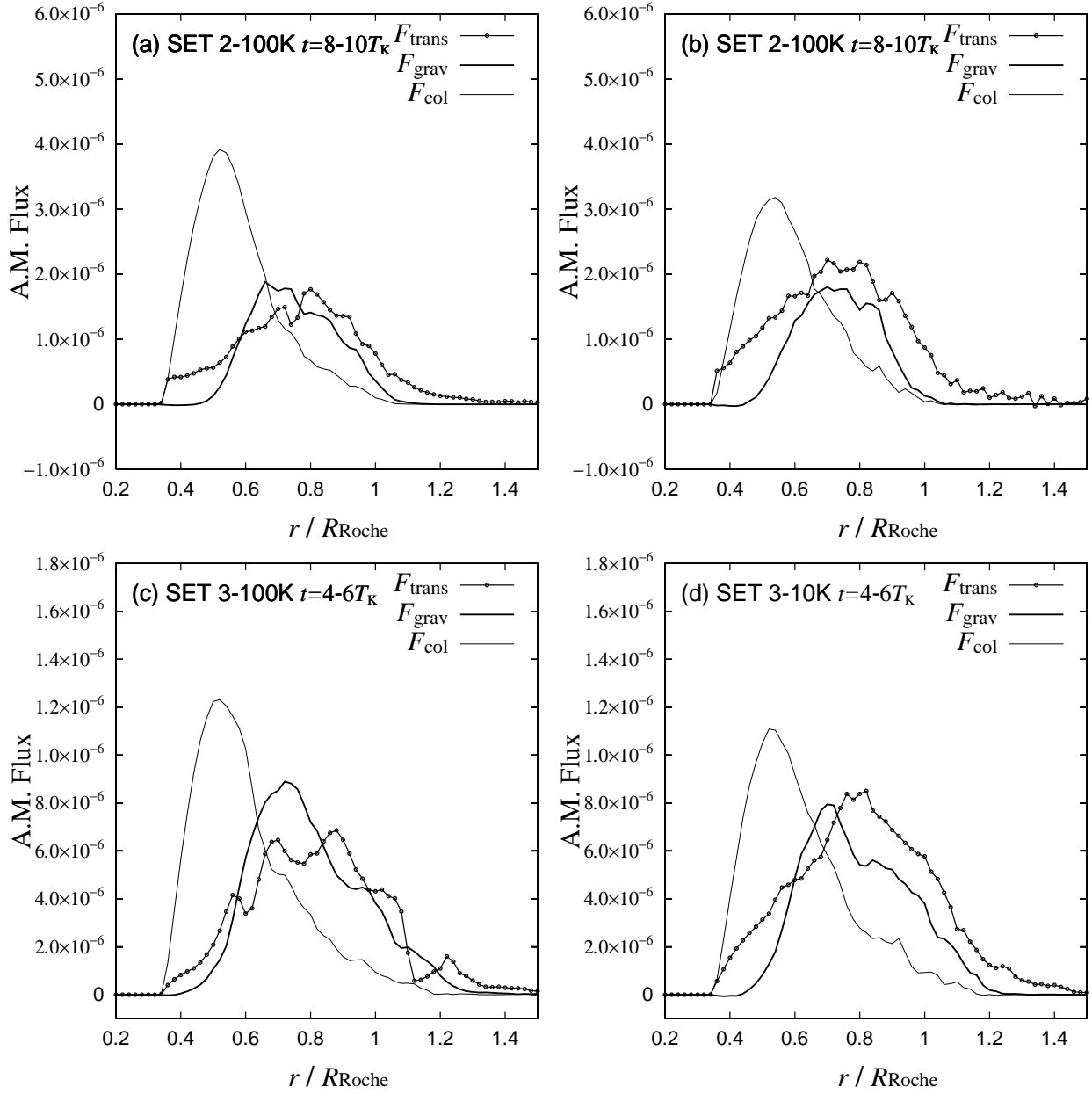
Figs.4



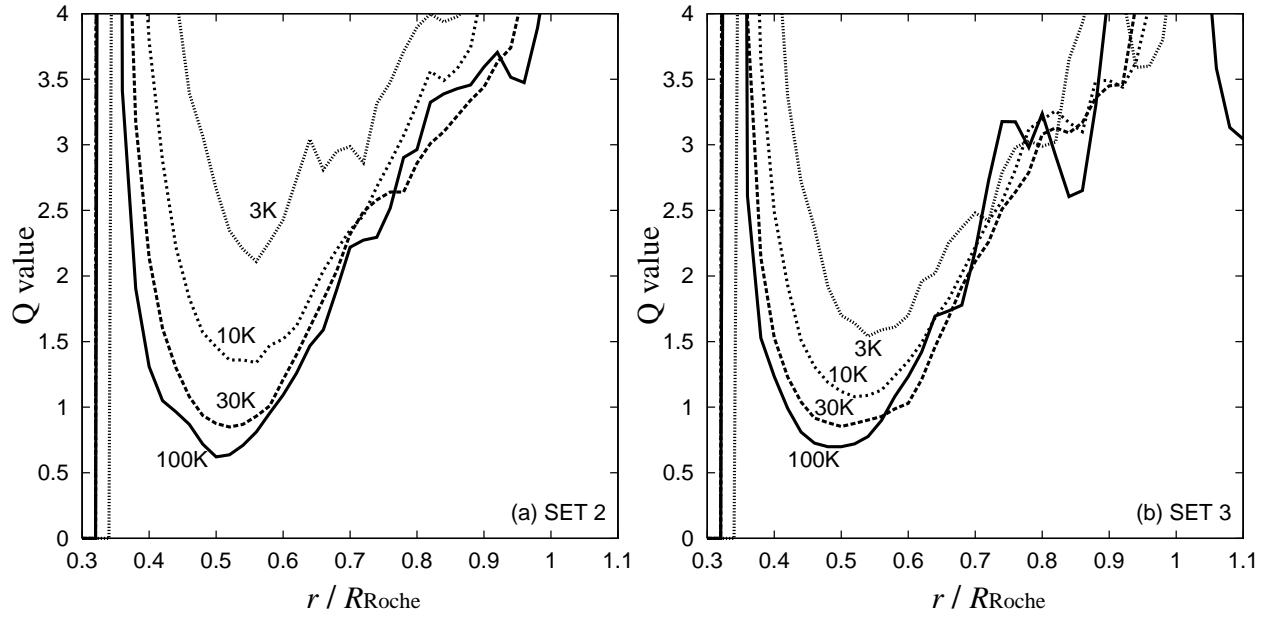
Figs. 5



Figs. 6



Figs.7



Figs. 8

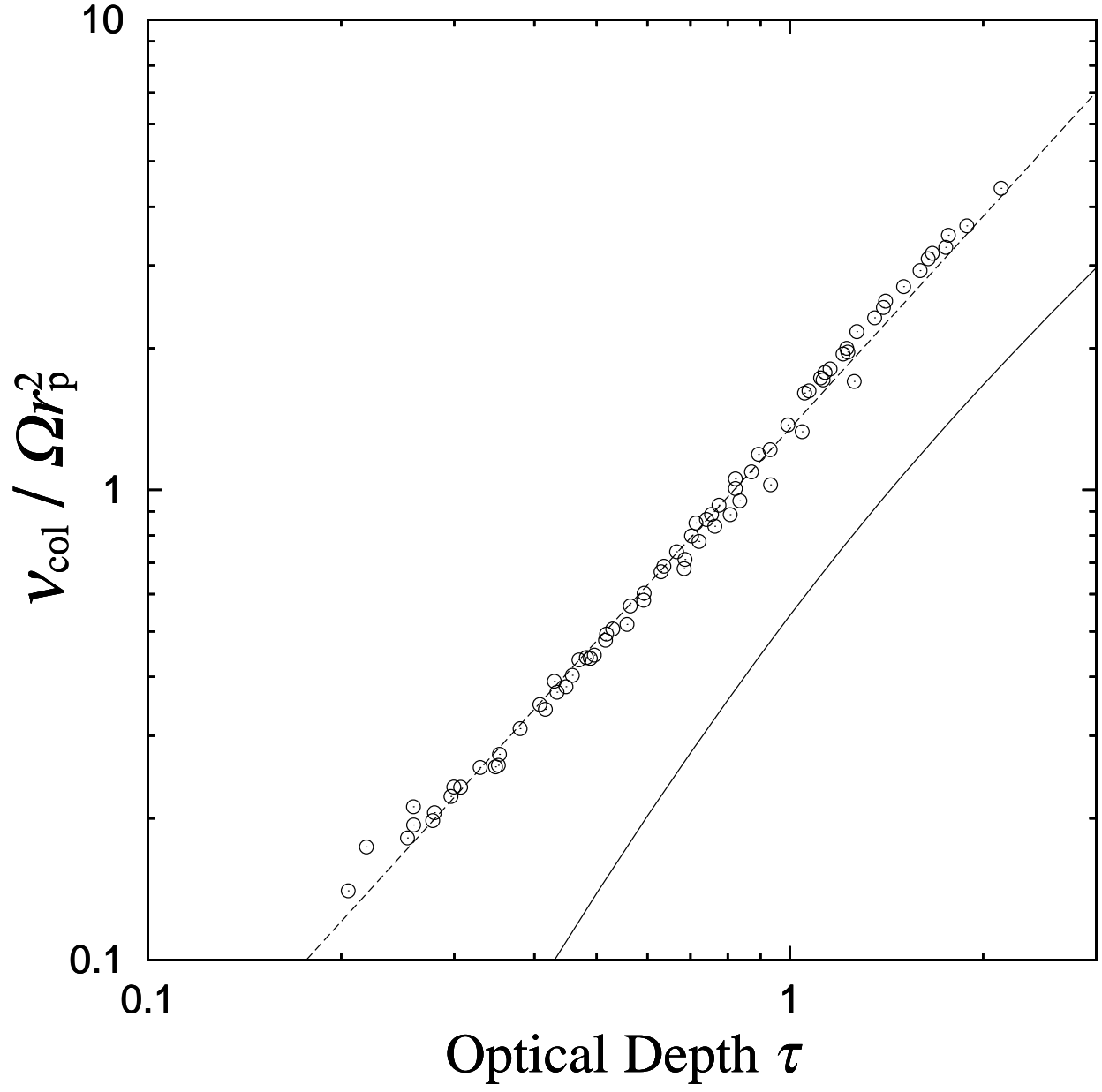
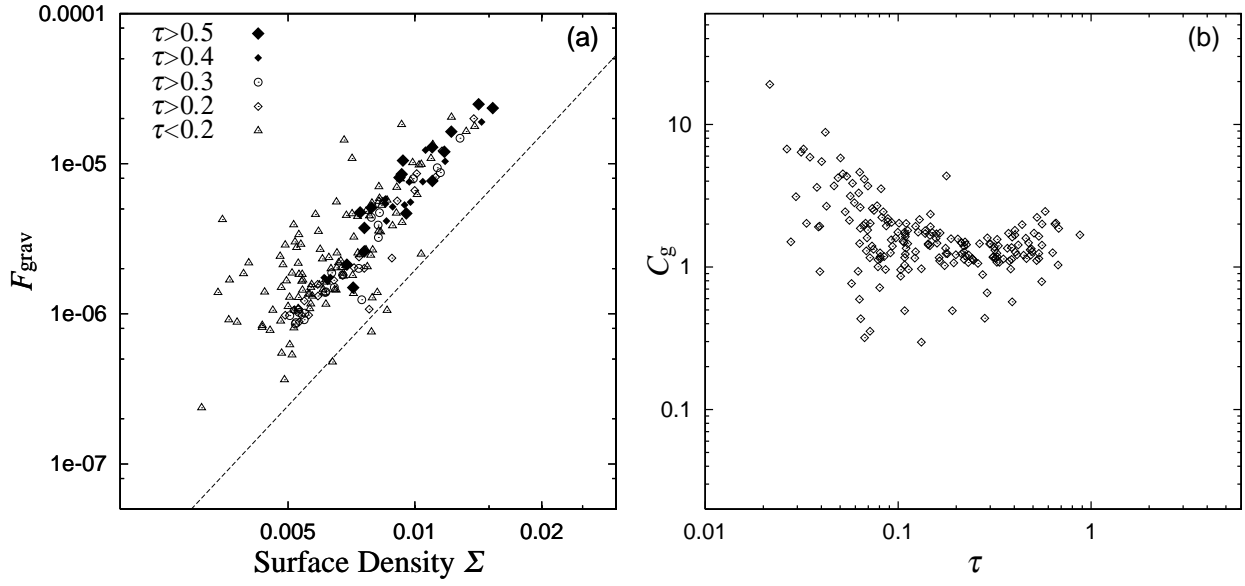
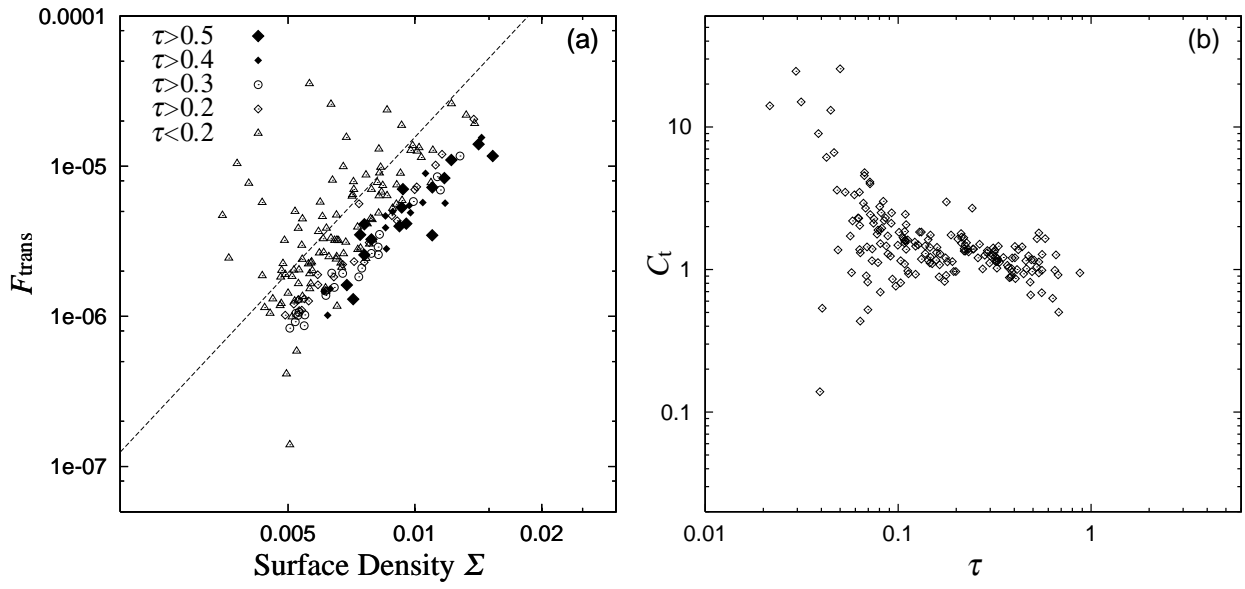


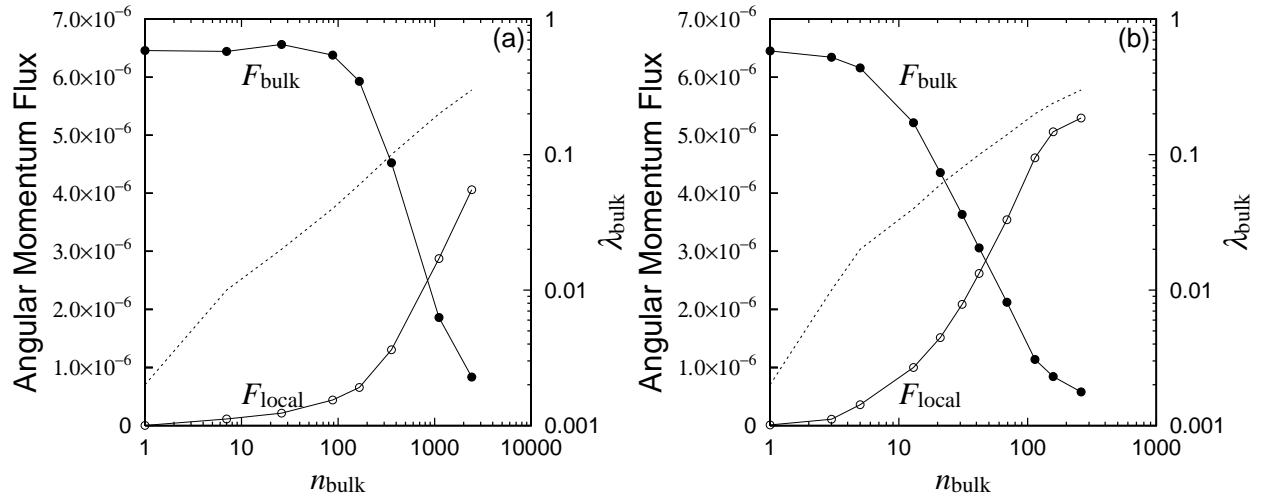
Fig.9



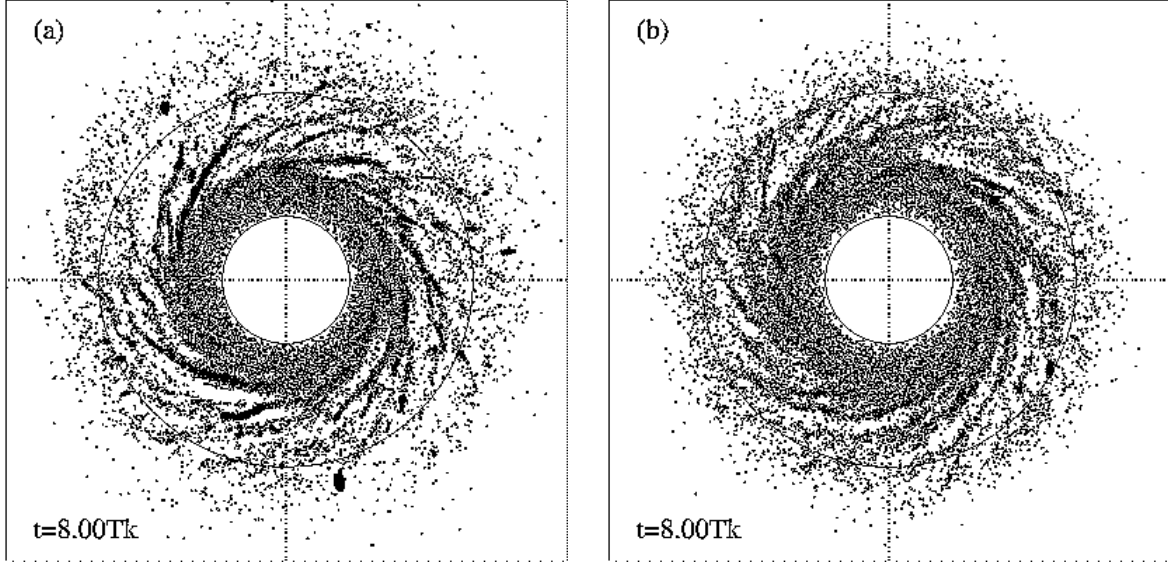
Figs. 10



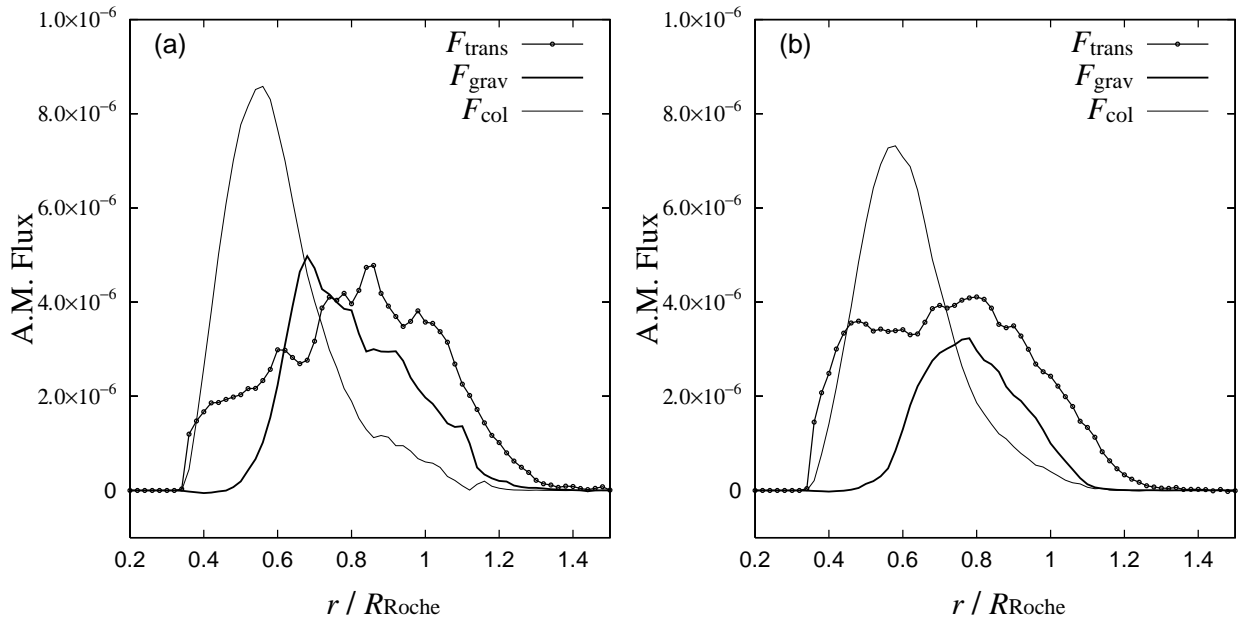
Figs. 11



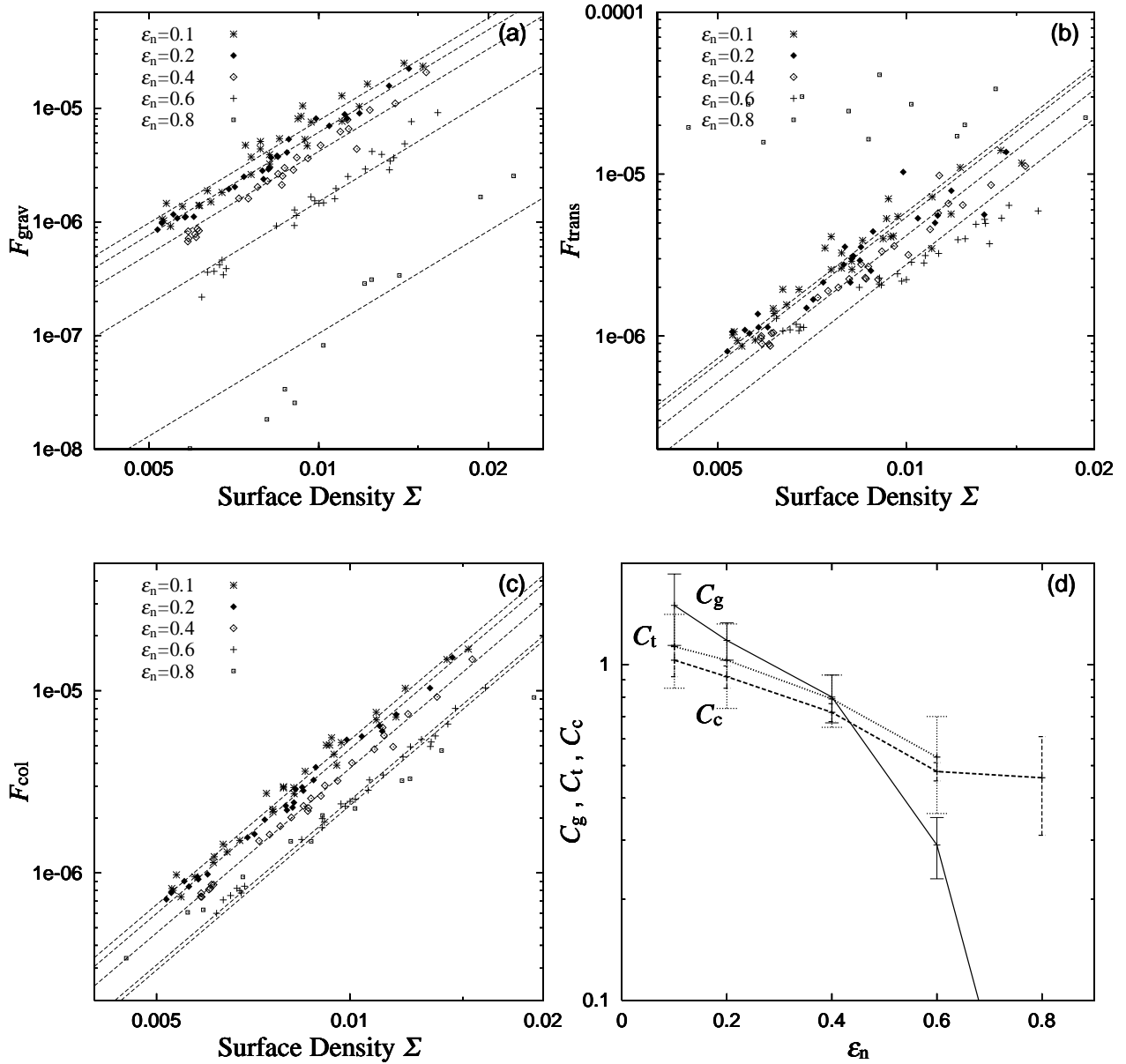
Figs. 12



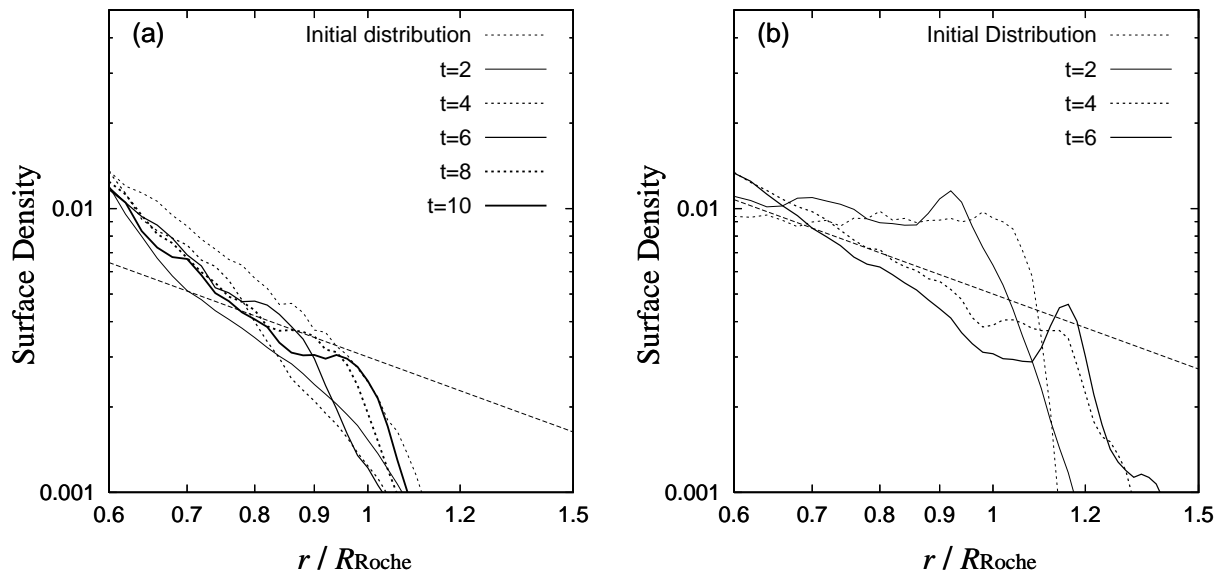
Figs. 13



Figs. 14



Figs. 15



Figs. 16